#### AADE-11-NTCE-73



### **Comprehensive Annular Flow Models for Drilling and Completions**

Wilson Chin and Xiaoying Zhuang, Stratamagnetic Software, LLC

Copyright 2011, AADE

This paper was prepared for presentation at the 2011 AADE National Technical Conference and Exhibition held at the Hilton Houston North Hotel, Houston, Texas, April 12-14, 2011. This conference was sponsored by the American Association of Drilling Engineers. The information presented in this paper does not reflect any position, claim or endorsement made or implied by the American Association of Drilling Engineers, their officers or members. Questions concerning the content of this paper should be directed to the individual(s) listed as author(s) of this work.

#### **Abstract**

Non-Newtonian flow in highly eccentric annuli with cuttings beds, washouts and fractures, encountered in cementing and drilling, are solved without crude slot flow and hydraulic radius approximations. The nonlinear formulation, written to customized, boundary-conforming, curvilinear coordinates providing high physical resolution in tight spaces, is solved exactly with no-slip conditions, and detailed velocities, apparent viscosities, shear rates and viscous stresses are computed for pressure drop and hole cleaning applications. For yield stress fluids, uncertainties related to plug zone size and shape are resolved using generalized Herschel-Bulkley relations applicable across transition boundaries (determined as part of the solution) reaching into and across plugs. Twodimensional, single-phase, steady flow simulations, solved rapidly using finite differences, provide detailed numbers and color displays for all physical quantities, with excellent numerical stability for all fluid types with and without yield Formulations for steady-state casing or drillpipe reciprocation and rotation are described, and extensions to model transient incompressible effects associated with starting, stopping and periodic movement, important in evaluating cement-mud displace efficiency, axial-helical cuttings transport, and jarring remedies for stuck pipe, are discussed. Detailed calculations showing the effect of rotation on flowrate or pressure gradient are given which highlight the crucial role of hole eccentricity.

#### Introduction

Non-Newtonian flows in highly eccentric annuli with cuttings beds, washouts and fractures, encountered in cementing and managed pressure (and underbalanced) drilling, are solved without crude slot flow and hydraulic radius approximations. The nonlinear partial differential equations, written to customized, boundary-conforming, curvilinear coordinate grid systems providing high physical resolution in tight spaces, are solved exactly with no-slip conditions, and detailed velocity, apparent viscosity, shear rate and viscous stress fields are computed for pressure drop, hole cleaning and other applications. For fluids with yield stress, well known uncertainties related to plug zone size and shape are fully resolved using Herschel-Bulkley relations applicable across transition boundaries (determined iteratively as part of the solution) reaching into and across the plug. Two-dimensional, single-phase, steady flow simulations, solved rapidly using finite difference methods, provide detailed numbers and color displays for all physical quantities within seconds, with excellent numerical stability for all fluid types with and without yield stress. Formulations for steady-state casing or drillpipe longitudinal translation and rotation are presented, and extensions to model transient incompressible effects associated with starting, stopping and periodic movement, important in evaluating cement-mud displacement efficiency, axial-helical cuttings transport, swab-surge, and jarring remedies for freeing stuck pipe, are developed. Practical problems are presented and the advantages over existing models are described. In this paper, extensive calculation methods and new modeling capabilities are presented for job planning, summarizing the approaches designed over the past two decades.

### **Background**

Annular flow modeling in boreholes, important to both drilling and cementing, is as old as petroleum engineering itself. In the simplest case, flow configurations are represented by concentric circles through which steady, two-dimensional, Newtonian and power law fluids flow; in these limits, exact analytical or numerical solutions of the flow equations provide useful tools for operational applications. For more complicated problems, e.g., eccentric annuli, non-ideal geometric irregularities, non-Newtonian yield stress fluids, pipe translation and rotation, however, numerous mathematical obstacles arise, which unfortunately introduce inefficiencies into field practices. We discuss these problems next

Geometric complications. In deviated and horizontal wells, heavy pipe and drill collar weight implies eccentric positioning within the borehole, as shown in (a) of Fig. 1, leading to difficulties in geometric description and solution. High eccentricities are often accompanied by non-symmetrical washouts, thick and irregularly formed cuttings beds, and possibly, fracture indentations. Early in petroleum engineering, the notion of a simple "mean hydraulic radius" permitting representation as an equivalent circular pipe flow, as depicted in (b) of Fig. 1, was widely employed; this approach, however, was not useful since what is meant by "mean" is not obvious and certainly not generally applicable from one situation to the next. Later "slot flow" models "unwrapped" the eccentric annulus, with the result as illustrated in (c) of Fig. 1, and then, further discretized the

resulting slot into local parallel plate elements, each of which is approximately modeled by simple solutions for fluid flow between ideal parallel plates. While somewhat reasonable, this approach applied strictly to very narrow annuli, but even then, curvature terms in the general governing momentum equations are always neglected. Thus, inertial effects are never properly modeled even in the limit of very narrow elements.

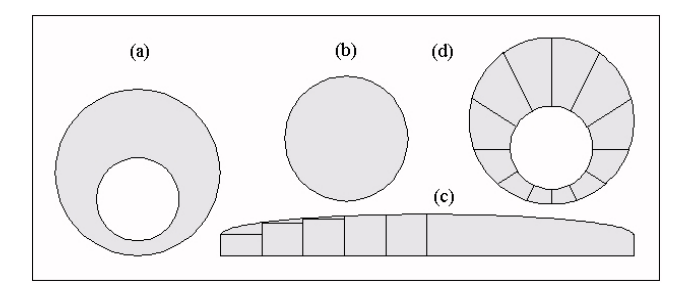


Fig. 1 – Idealizations commonly used to represent eccentric borehole annuli.

Improvements to slot flow models are provided by "pie slice" formulations, idealized in (d) of Fig. 1, in which eccentric annuli are represented by "pie slices" of varying size and included angle having the pipe center as a virtual origin. The solution for each slice is taken from the numerical solution for a concentric annular problem with a closely matched radius. In this approach, pie slices ranging from small to large are used. However, it is clear from the sketch that perfect geometric matching of the borehole boundary is never completely achieved, so that adequate modeling of curvature effects is approximate at best. Moreover, the concentric solutions used are numerical in the case of yield stress fluids and awkward in implementation. More recently, authors have used "bipolar coordinates" to represent eccentric circles, and while these provide useful host formulations for zero-vield-stress fluids, the algebra required to represent even the simplest non-Newtonian flow problems is overwhelming compared to the methods introduced later. The mapping method used in the present paper, it turns out, provides superior modeling capabilities in that the complete momentum equation for any rheology and annular geometry can be solved exactly. The new approach is less intensive numerically and easily describes realistic cuttings beds, washouts and fracture indentations.

Geometric difficulties, however, are much more than what meets the eye. When yield stress fluids flow, "plug regimes" that move as solid bodies are always present in flow domains below a given yield stress. When slot flow or pie slice models are used to simplify the solution process, "plug rings" are always obtained by virtue of the adhoc recipes described above. This is physically incorrect in most operational situations characterized by high eccentricity. For example, one would expect a large, isolated, almost circular plug element at the wide side of (a) of Fig. 1 and perhaps in a narrow strip at the bottom, but a flow containing such a solid plug would be ruled out by both solution methods. Until

recently, of course, exact solutions for (a) Fig. 1 with yield stress fluids, e.g., Bingham plastics and Herschel-Bulkley models, were impossible anyway for one important reason – theoretically, the size and shape of the plug zone are unknown in problems without azimuthal symmetry, and without knowledge of these internal boundary properties, a complete flow solution could not be obtained. This paper addresses and solves this problem in its complete generality.

Mathematical difficulties. Ideally, one would represent the details of highly eccentric annular domains exactly and in their entirety using boundary-conforming, curvilinear meshes, to which the governing equations of motion would be written, solved, and post-processed for relevant engineering information. However, this is often numerically difficult because there are as many distinct partial differential equation formulations as there are fluid rheologies, e.g., the equations for Newtonian, power law, Bingham plastic and Herschel-Bulkley fluids are very different, each with its own convergence, stability and physical properties. because the equations are generally nonlinear, solutions must be obtained by iterative means. In fact, iterative solutions solving complicated grid generation equations must be followed by iterative solutions to produce the required flowfields on the resulting meshes. These difficulties are compounded, typically, by user inexperience in computational grid generation and numerical analysis. Even when solutions to underlying velocity fields are available, post-processed field solutions for shear rate, viscous stress, apparent viscosity, and so on, need to be automated and rapidly displayed in order to be useful in real-time applications. This requirement is particularly relevant in ultra-deepwater applications since fast and accurate pressure solutions are required to navigate the narrow window between formation fracture and disastrous blowout. These problems are all addressed in the software development program.

**User interface considerations.** Assuming that both geometric and mathematical issues can be addressed satisfactorily, human factors issues relating to software usage become all-important especially in anticipated applications to managed pressure drilling in ultra-deepwater drilling and holecleaning at high deviation angles. Physical formulations must be mathematically rigorous, numerical solutions must be detailed and pertinent to the annular geometry at hand, and complete field solutions for all engineering properties must be achievable in a manner that is completely transparent to typical engineering users with undergraduate degrees – and, even better, to field technicians with minimal modeling experience or mathematical training. This requires fully automatic grid generation, nonlinear equation setup and stable matrix inversion.

The user interface must be designed with rigsite workflows in mind. Importantly, accuracy and speed, that is, "desktop speed" from problem definition to automated color displays, go hand-in-hand, because of demands imposed by narrow margins between pore-pressure and fracture-pressure gradient profiles in modern offshore applications. All of the above considerations, again, accurate geometric modeling,

rigorous mathematical formulation and solution, and fast, user-friendly, graphically-oriented software implementation, render the general annular flow modeling problem extremely challenging. We now address each of the foregoing issues and explain how the solutions satisfactorily address these needs.

#### **Exact Geometric and Mathematical Formulation**

Boundary-conforming, curvilinear meshes. Coordinate systems "natural" to engineering problems play vital roles in facilitating efficient and accurate computational solutions. For example, circular coordinates are natural to circular wells producing from infinite reservoirs, while rectangular systems are ideal for problems solving, say, temperature distributions on rectangular plates. By the same token, a mesh system suitable for eccentric annular geometries would have inside coordinate lines that coincide with circular or square drill collars with stabilizers, while outside lines would conform to irregular borehole walls with their cuttings beds, washouts and fracture indentations. A second set of coordinate lines might be constructed orthogonally to the first, although this is not necessary if all terms in the resulting transformed governing equations are retained. By contrast, it is clear that rectangular (x,y) or circular  $(r,\theta)$  coordinates are less than satisfactory for accurate geometric description of general annuli.

In natural "boundary-conforming, curvilinear coordinates," here denoted by  $(\xi,\eta)$ , boundary conditions would be easily specified. For example, the no-slip velocity condition for stationary surfaces, say, at pipe and borehole surfaces, is simply described by "u=0" along horizontal grid lines  $\xi=\xi_{pipe}$  and  $\xi=\xi_{borehole}$  where the subscripted numbers are constants. By contrast, the formulation in rectangular coordinates would require u=0 applied along cumbersome curves, e.g.,  $u\{x,f(x)\}=0$  where y=f(x) represents internal and external contours.

The objective behind grid generation is a set of transformations  $\xi(x,y)$  and  $\eta(x,y)$  that enable simple boundary condition implementation, so that a complicated physical region, here the eccentric borehole annulus, becomes a simple rectangular one in a computational domain, where the solution of the mathematical problem is undertaken. Once the mapping transforms are available, the governing equation itself must be expressed in the new coordinates. For example, the partial differential equation for steady-state, two-dimensional, Newtonian fluid flow is the well known  $u_{xx} + u_{yy} = -\mu^{-1} \partial P/\partial z$  where  $\mu$  and  $\partial P/\partial z$  represent viscosity and applied pressure gradient. Although this appears in rectangular coordinates, the equation applies to all annular geometries.

The conversion process itself is straightforward. Suppose we wish to express a function u(x,y) in terms of convenient independent variables  $\xi$  and  $\eta$ . If the transformations  $x = x(\xi,\eta)$  and  $y = y(\xi,\eta)$  are available, direct substitution allows us to rewrite u(x,y) in the form  $u(x,y) = U(\xi,\eta)$ , where the functional relation  $U(\xi,\eta)$  between  $\xi$  and  $\eta$  is generally different from the relation u(x,y) connecting x and y. Derivatives of u(x,y) with respect to x and y are easily

related to derivatives of  $U(\xi,\eta)$  taken with respect to  $\xi$  and  $\eta$ . For example, it is easily shown that  $U_\xi = u_x x_\xi + u_y \ y_\xi$  and  $U_\eta = u_x x_\eta + u_y \ y_\eta$  for the first derivatives, with obvious extensions to second derivatives obtained using the chain rule of calculus. In general fluid-dynamical problems, the resulting equation for  $U(\xi,\eta)$  is typically more complicated than that for u(x,y). The computational benefit, however, is accurate and noise-free implementation of boundary conditions, not to mention the use of much fewer grid points for the same level of physical resolution. Calculated solutions are displayed in physical space with the assistance of custom color plotting routines.

Many commercial simulators calculate velocities and other flow properties directly using rectangular (x,y) grids. We emphasize that x-y coordinate lines do not conform to the irregular curves defining near and farfield boundaries; also, high grid densities imposed, say at the bottom of an eccentric annulus, would require similarly high densities far away where detailed resolution is unnecessary. This results in large, inefficient computing domains containing dead flow and extremely large matrices. In addition, "choppy" meshes lead to noise, inaccuracy and instability. Other simulators, particularly general purpose codes used in computational fluid dynamics (CFD), do support automatic and efficient "finite element" or "finite volume" gridding. However, they are not portable in the sense that special licenses must be purchased for users, thus incurring significant costs. But more importantly, they run proprietary, high-overhead "canned" routines that cannot be adapted to new mathematical models (such as the novel yield stress formulation introduced below) and cannot be "tuned" to run optimally. Also, they offer inflexible output formats that are not easily integrated with custom designed graphics and user interface software. In this paper, the objective is a fast, flexible and accurate solution procedure that can be installed on all operating systems at minimal cost.

We conceptually describe the grid generation process in this paper. Details are offered in Chin (1992, 2001, 2002). We reiterate the basic ideas here because they are essential to understanding the solution approach and its topological advantages. Rather than dealing directly with  $\xi = \xi(x,y)$  and  $\eta = \eta(x,y)$ , we equivalently consider the inverse functions  $x = x(\xi,\eta)$  and  $y = y(\xi,\eta)$  satisfying *nonlinear* coupled partial differential equations, which are derived in the form

$$\begin{split} &(x_{\eta}^{\ 2}+y_{\eta}^{\ 2})\,x_{\xi\xi}\,\text{-2}\,(x_{\xi}x_{\eta}+y_{\xi}y_{\eta})\,x_{\xi\eta}\,+(x_{\xi}^{\ 2}+y_{\xi}^{\ 2})\,x_{\eta\eta}\,=0\quad(1)\\ &(x_{\eta}^{\ 2}+y_{\eta}^{\ 2})\,y_{\xi\xi}\,\text{-2}\,(x_{\xi}x_{\eta}+y_{\xi}y_{\eta})\,y_{\xi\eta}\,+(x_{\xi}^{\ 2}+y_{\xi}^{\ 2})\,y_{\eta\eta}\,=0\quad(2) \end{split}$$

where  $\xi$  and  $\eta$  are now independent (as opposed to dependent) variables. We aim to map the irregular flow domain of Fig. 2a into the simple rectangular computational domain of Fig. 2b where  $B_1$  and  $B_2$  are physically insignificant "branch cuts" where single-valued solution constraints are enforced.

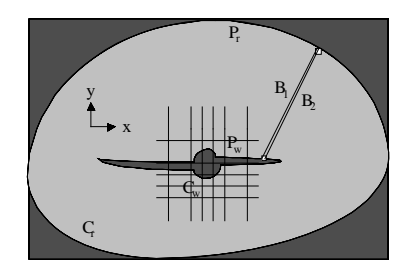


Fig. 2a – Irregular physical domain with inefficient rectangular meshes.

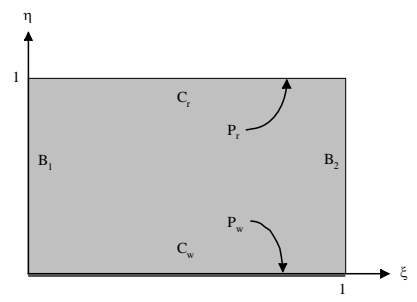


Fig. 2b – Irregular domain mapped to rectangular computational space.

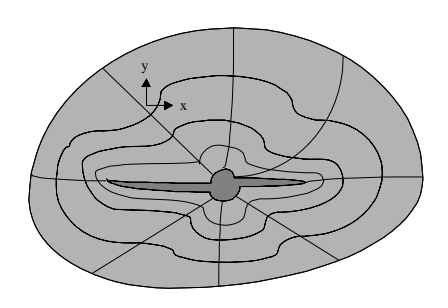


Fig. 2c - Physical domain in boundary-conforming coordinates.

How are the foregoing equations used to create numerical mappings? Suppose that contour  $C_W$  in Fig. 2a is to map into  $\eta=0$  of Fig. 2b. The user first discretizes  $C_W$  in Fig. 2a by penciling along it a sequence of dots chosen to represent the curve. If these are selected in an orderly, say, clockwise fashion, they define the direction in which  $\xi$  increases. Along  $\eta=0$ , values of x and y are known (e.g., from measurement on graph paper) as functions of  $\xi$ . Similarly, x and y values along  $C_r$  are known as functions of  $\xi$  on  $\eta=1$  of Fig. 2b. These provide the boundary conditions for Eqs. 1 and 2, which are augmented by single-valuedness constraints at arbitrarily chosen branch cuts  $B_1$  and  $B_2$ . It is clear that this process is easily automated by computer.

Conventionally, in grid generation, Eqs. 1 and 2 are discretized by finite differences and solved by point or line relaxation, starting with guesses for the dependent variables x and y. The problem is linearized by approximating all nonlinear coefficients using values from earlier iterations. Typically, several updates to Eq. 1 are taken, followed by updates to Eq. 2, with this cycling process, often unstable, repeated continuously until convergence. Variations of the

approach are known, with  $100 \times 100$  mesh systems in the  $\xi$ - $\eta$  plane requiring minutes of computing time. Once  $x = x(\xi,\eta)$  and  $y = y(\xi,\eta)$  are solved and tabulated as functions of  $\xi$  and  $\eta$ , physical coordinates are generated. First,  $\eta$  is fixed; for each node  $\xi$  along this  $\eta$ , computed values of (x,y) pairs are successively plotted in the x-y plane to produce the required closed contour. This procedure is repeated for all values of  $\eta$ , until the entire family of closed curves is obtained, with limit values  $\eta = 0$  and  $\eta = 1$  again describing  $C_w$  and  $C_r$ . Orthogonals are constructed by repeating the procedure, with  $\eta$  and  $\xi$  roles reversed.

This process provides the curvilinear mapping only. The equation describing the physics (e.g., the Navier-Stokes equation for Newtonian flow or the general rheological equations for non-Newtonian fluids) must be transformed into  $(\xi,\eta)$  coordinates and solved. In general, the transformed governing equation, which is algebraically more complicated, must be solved, and this procedure introduces its own complications and numerical challenges. The "simplification," however, lies not in the transformed equation, which now contains mixed derivatives and variable coefficients, but in the computational domain itself, because this domain takes on a rectangular form amenable to simple, noise-free numerical solution, requiring significantly fewer nodal points for high resolution physical definition.

Again, existing solution methods solving  $x(\xi,\eta)$  and  $y(\xi,\eta)$  stagger the solutions for Eqs. 1 and 2. For example, crude solutions are used to initialize the coefficients of Eq. 1, and improvements to  $x(\xi,\eta)$  are obtained. These are used to evaluate the coefficients of Eq. 2, in order to obtain an improved  $y(\xi,\eta)$ ; then, attention turns to Eq. 1 again, and so on, until convergence is achieved. Various over-relaxation means are used to implement these iterations, e.g., point SOR, line SLOR, line SOR with explicit damping, alternatingdirection-implicit, and multigrid, with varying degrees of (Note that "SOR" and "SLOR" denote the success. "successive-over-relaxation" "successive-line-overand relaxation" methods used to solve partial differential equations iteratively in the numerical analysis literature.) Often these schemes diverge computationally. In any event, the staggering used introduces different artificial time levels while iterating. Classic numerical analysis, however, suggests that faster convergence and improved stability are possible by reducing the number of time levels.

A new approach to rapidly solve the nonlinear coupled grid generation equations was proposed earlier and is based on a very simple idea. This idea has since been validated in numerous applications. Consider first  $z_{\xi\xi}+z_{\eta\eta}=0,$  for which  $z_{i,j}\approx(z_{i-1,j}+z_{i+1,j}+z_{i,j-1}+z_{i,j+1})/4$  holds on constant grid systems (this is easily derived using standard finite difference formulas). This well-known averaging law motivates the  $recursion\ formula\ z_{i,j}^n=(z_{i-1,j}^{n-1}+z_{i+1,j}^{n-1}+z_{i,j+1}^{n-1})/4$  often used to illustrate and develop multilevel iterative solutions; an approximate, and even trivial solution, can be used to initialize the calculations, and nonzero solutions are always produced from nonzero boundary

conditions.

But the well-known Gauss-Seidel method is fastest: as soon as a new value of  $z_{i,j}$  is calculated, its previous value is discarded and overwritten by the new value. This speed is accompanied by low memory requirements, since there is no need to store both n and n-1 level solutions: only a single array,  $z_{i,j}$  itself, is required in programming. The approach to Eqs. 1 and 2 was motivated by the following idea. Rather than solving for  $x(\xi,\eta)$  and  $y(\xi,\eta)$  in a staggered, leap-frog manner, is it possible to *simultaneously* update x and y in a similar once-only manner? Are convergence rates significantly increased? What formalism permits us to solve in Gauss-Seidel fashion? What are the programming implications?

$$(z_{\eta}\,z_{\eta}^{\,\,*})\,z_{\xi\xi}\,\text{-}\,(z_{\xi}\,z_{\eta}^{\,\,*}+z_{\xi}^{\,\,*}z_{\eta}^{\,\,})\,z_{\xi\eta}^{\,\,}+(z_{\xi}\,z_{\xi}^{\,\,*})\,z_{\eta\eta}^{\,\,}=0\ (3)$$

This form yields significant advantages. First, when z is declared as a complex variable in a Fortran program, Eq. 3 represents, for all practical purposes, a single equation in  $z(\xi,\eta)$ . There is no need to leap-frog between x and y solutions now, since a single formula analogous to the classical model  $z_{i,j}=(z_{i-1,j}+z_{i+1,j}+z_{i,j-1}+z_{i,j+1})/4$  is easily written for the  $z_{i,j}$  using Eq. 3 as the host equation. Because both x and y are simultaneously resident in computer memory, the extra time level present in staggered schemes is completely eliminated, as in the Gauss-Seidel method. In thousands of test simulations conducted using point and line relaxation, convergence times are shorter by orders of magnitude relative to those obtained for cyclic solution between  $x(\xi,\eta)$  and  $y(\xi,\eta)$ . Convergence appears to be unconditional, monotonic and stable. Because Eq. 3 is nonlinear, von Neumann tests for exponential stability and traditional estimates for convergence rate do not apply, but the evidence for stability and convergence, while empirical, remains very strong and convincing since we have always computed useful grids in all test runs.

Iterative solution of nonlinear partial differential equations. Earlier we noted that  $u_{xx} + u_{yy} = -\mu^{-1} \partial P/\partial z$  applies to steady, two-dimensional, single-phase Newtonian flows for borehole annuli having the most complicated shapes; unfortunately, practical solutions cannot be accurately obtained in (x,y) coordinates. Here,  $\mu$  is a constant viscosity and  $\partial P/\partial z$  is the applied pressure gradient in the z direction assumed to be known. This is the so-called Poisson equation in mathematics, and students who have undertaken its study realize that, despite the apparent simplicity offered by few

terms and complete linearity, useful solutions to the classical model are nonetheless difficult to obtain. When the underlying fluid is nonlinear, this equation is replaced by Eq. 4, which is vastly more complicated, that is,

$$\partial (N \partial u/\partial y)/\partial y + \partial (N \partial u/\partial x)/\partial x = \partial P/\partial z \tag{4}$$

where N now represents the "apparent viscosity" function. This apparent viscosity is not constant, but a function of local shear rates whose mathematical form depends on the particular rheology assumed. For example, in the case of power law fluids modeled by an exponent "n" and a consistency factor "K," N takes the form  $N = K [(\partial u/\partial y)^2 + (\partial u/\partial x)^2]^{(n-1)/2}$ . Even without solving the problem, it is clear that, since  $\partial u/\partial x$  and  $\partial u/\partial y$  depend on the (unknown) solution itself, any resulting apparent viscosity must vary locally within the flow domain and depend on both geometric details and flow rate. Detailed computed solutions for annular flows are presented in Chin (1992, 2001) where approximate approaches to plug flow modeling are used.

Because Eq. 4 is now strongly nonlinear, the solution process at its very heart must remain nonlinear. This implies that one cannot use simpler Newtonian solutions as leading approximations and focus on higher order improvements to them. The basic solution method must retain a fully nonlinear character in order that well known nonlinear relationships between pressure gradient and volume flow rate evolve as part of an iterative computational process. As if this alone were not complicated enough, we emphasize that it is the reexpression of Eq. 4 in general  $(\xi,\eta)$  curvilinear coordinates, not in simple (x,y) coordinates, that must be solved, and that these coordinates and their metrics are only available numerically.

The transformed equation now contains additional terms as well as nonlinear coefficients that depend on the mapping. Direct solutions are not numerically possible, but exact solutions can be obtained iteratively. In fact, finite difference methods are used; the solutions are obtained line-by-line using so-called "successive line over relaxation" (SLOR) schemes written in the curvilinear coordinates. These iterative solutions are initialized by "close" analytical or numerical solutions; the closer the initial guess, the more rapid the convergence. For typical problems, the efficient schemes devised will produce a usable curvilinear grid in approximately one second of computing time, while the solution of the transformed momentum equation (when pressure gradient is specified) may require two-to-three seconds. Again, detailed discussions and computed solutions for power law and simple plug flows in highly eccentric annuli, with practical applications, are given in Chin (1992, 2001). The approximate plug flow methods developed in these early researches are now obsolete and are replaced by the following exact approach for yield stress description and modeling.

Yield stress, plug zone size and shape modeling. In fluid flows where yield stresses exist, "plug zones" are to be found. These plugs move as solid bodies within the flowing

system. For pipes with circular cross-sections and for concentric annuli, it is possible to derive exact analytical solutions for plug zone size and shape for Bingham plastics (general solutions have, in fact, been derived for both geometries assuming Herschel-Bulkley fluids, and will be presented separately). For circular pipes, the cross-sectional plug is simply a circle; for concentric annuli, of course, the plug is a concentric ring.

The appearance of solid plugs within moving streams results from the rheological model used by mathematicians to idealize the physics. If we denote the shear rate functional by  $\Gamma = [\ (\partial u/\partial y)^2 + (\partial u/\partial x)^2\ ]^{1/2}, \text{ this idealization can be written formally as}$ 

$$\begin{split} N &= k \; \Gamma^{n-1} + S_{yield} / \Gamma \; \text{if} \; \{1/2 \; \text{trace} \; (\underline{\underline{S}} \bullet \underline{\underline{S}})\}^{1/2} > \tau_0 \\ \underline{\underline{D}} &= 0 \; \text{if} \; \{1/2 \; \text{trace} \; (\underline{\underline{S}} \bullet \underline{\underline{S}})\}^{1/2} < \tau_0 \end{split} \tag{5}$$

where the general extra stress tensor is denoted by  $\underline{\mathbf{S}}$  and the deformation tensor is given by  $\underline{\mathbf{D}}$ . Here,  $\tau_0$  is the so-called "yield stress." The discontinuous "if, then" character behind Eq. 5 is responsible for the sudden transition from shear flow to plug flow commonly quoted. As noted, for flows with azimuthal symmetry, that is, circular pipes and concentric annuli, exact, rigorous mathematical solutions are in fact possible.

For non-circular ducts and eccentric annuli, which describe a large number of practical engineering problems, it has not been possible to characterize plug zone size and shape, even approximately. Thus, the most significant petroleum engineering flow problems important to both drilling and cementing cannot be modeled at all, let alone accurately. In order to remedy this situation, we observe that the discontinuity offered in Eq. 5 is really an artificial one, introduced for, of all reasons, "simplicity." This unfortunately leads to the solution difficulties noted. In reality, practical engineering flows do not suddenly turn from shear to plug flow; the transition may be rapid, but it will occur continuously over finite measurable distances. We therefore turn to more realistic rheological models which apply continuously throughout the entire problem domain, and which, if the underlying flow parameters permit, lead to plug zones naturally during the solution process.

The conventional Herschel-Bulkley viscoplastic model, which includes Bingham plastics as a special limit when the exponent "n" is unity, requires that  $\tau=\tau_0+K(d\gamma/dt)^n$ , if  $\tau>\tau_0$  and  $d\gamma/dt=0$  otherwise. Here  $\tau$  is the shear stress,  $\tau_0$  is the yield stress, K is the consistency factor, n is the exponent, and  $d\gamma/dt$  is the shear rate. As explained, this model is far from perfect. For example, both Herschel-Bulkley and Bingham plastic models predict infinite viscosities in the limit of vanishing shear rate, a fact that often leads to numerical instabilities. In addition, the behavior is not compatible with conservation laws that govern many complex flows.

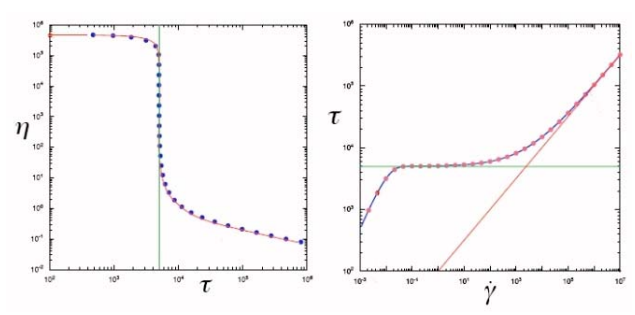


Fig. 3 - Extended Herschel-Bulkley law.

An alternative to the standard Herschel-Bulkley model is the use of continuous functions which apply to sheared regimes, and in addition, through and into the plug zone. One such example model is suggested by Souza, Mendez and Dutra (2004), that is,  $\tau = \{1 - \exp(-\eta_0 \ d\gamma/dt \ /\tau_0)\}\{\tau_0 + K \ (d\gamma/dt)^n\}$ , which would apply *everywhere* in the problem domain. The corresponding apparent viscosity N, for numerical implementation in Eq. 4, is denoted by

$$\begin{split} \eta &= \tau \, / (d\gamma \, / dt) \\ &= \{1 - exp(-\eta_0 \, d\gamma / dt \, / \tau_0)\} \{\tau_0 / (d\gamma / dt) + K \, (d\gamma / dt)^{n-1}\} \end{split} \tag{6}$$

The "apparent viscosity vs shear stress" and "shear stress vs shear rate" diagrams, from Souza et al, are duplicated in Fig. 3. What are the physical consequences of this model? Eq. 6, in fact, represents an "extended Herschel-Bulkley" model in the following sense. For infinite shear rates, one would recover  $\tau = \tau_0 + K (d\gamma/dt)^n$ . But for low shear rates, a simple Taylor expansion leads to  $\eta \approx \{\eta_0(d\gamma/dt)/\tau_0\}\{\tau_0/(d\gamma/dt) + K$  $(dy/dt)^{n-1}$   $\approx \eta_0$  where it is clear now that  $\eta_0$  represents a very high viscosity for the plug zone. The use of Eq. 6 in numerical algorithms simplifies both formulation and coding since internal boundaries and plug domains do not need to be determined as part of the solution. A single constitutive law (as opposed to the use of two relationships in Eq. 5) applies everywhere, thus simplifying computational logic; moreover, the continuous function assumed also possesses continuous derivatives everywhere and allows the use of standard difference formulas. Cumbersome numerical matching across internal boundaries is completely avoided. In a practical computer program, the plug zone viscosity might be assumed, for example, as 1,000 cp. In fact, we choose high values of  $\eta_0$ which would additionally stabilize the numerical integration schemes used. This strategy is applied throughout this work, both to the iterative relaxation schemes for steady-state problems and to the transient integration schemes for more complicated formulations. This new approach was first discussed in Chin and Zhuang (2010) for steady flows and has since been incorporated in the fully transient annular flow modeling approaches.

**Borehole axis radius of curvature.** Borehole axis curvature is important to ultra-deepwater drilling, especially in short and medium radius turning applications. Several aspects of cuttings transport and debris removal are not completely understood insofar as centrifugal effects are concerned and a

study of curvature effects contributes to an understanding of their influence on stress fields. Also, bends in pipelines and annuli are interesting because they are associated with losses; that is, to maintain a prescribed volume flow rate, a greater pressure drop is required in pipes with bends than those without. This is true because the viscous stresses acting along pipe walls are higher. The modeling of borehole axis curvature effects for problems involving noncircular ducts and highly eccentric annuli containing non-Newtonian fluids was first addressed in Chin (2001), where detailed derivations, equations and computed examples are given. Essentially, it is shown how, by replacing " $1/\mu$   $\partial P/\partial z$ " with an inertially corrected " $1/\mu \partial P/\partial z - 1/R \partial u/\partial r + u/R^2$ " where R is the radius of curvature, the effective pressure gradient accounting for centrifugal effects is properly and stably modeled. This model is incorporated into Eq. 4 and a radius of curvature entry appears in the software menu in Fig. 4a at the bottom left.

### Steady and Transient Formulations: User Interface and Physical Modeling Capabilities

Simulators for two-dimensional steady and transient flow are described in this paper, applicable to single-phase, Herschel-Bulkley fluids, which may also be operated in Newtonian, power law and Bingham plastic modes. For Bingham plastic and Herschel-Bulkley fluids, the generalized rheological approach is used and plug zone sizes and shapes are determined automatically whatever the eccentric annular The intuitive user interface shown in Fig. 4a geometry. requires only an elementary understanding of engineering vocabulary and the simulator may be operated with minimal training. Annular geometry is defined by entering center coordinates and radii in the upper left menu. Clicking 'Show Annulus' provides an instantaneous display of the geometry assumed, plus a typical curvilinear grid, e.g., as illustrated in Fig. 4b, whose mesh density may be coarsened or refined at In addition, online editing utilities allow the baseline eccentric circles to be edited for washout, cuttings bed or fracture modification effects.

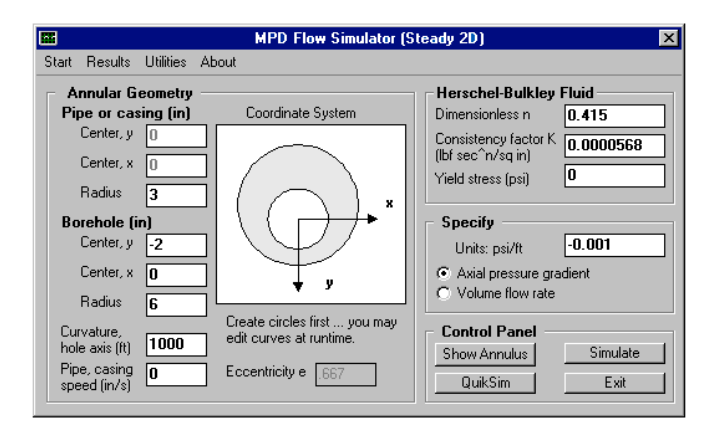


Fig. 4a - Steady flow user interface.

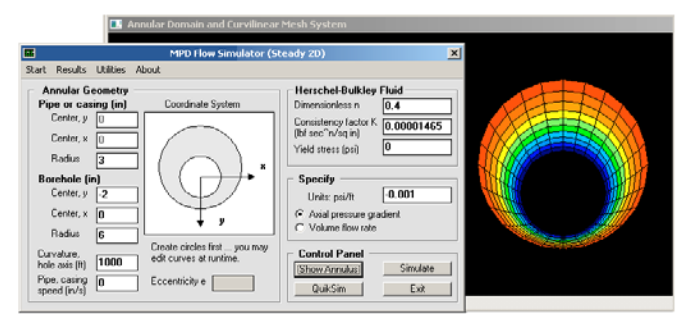


Fig. 4b – Quick annular geometry and curvilinear grid display mode.

Rheological parameters for the general Herschel-Bulkley fluid are entered into the input boxes at the upper right of Fig. 4a. Four model are possible by choosing the values of n, K and  $\tau_0$  appropriately. Newtonian fluids require n=1 and  $\tau_0=0$ , while power law fluids allow general n with vanishing  $\tau_0$ . On the other hand, Bingham plastics require n=1 and non-vanishing  $\tau_0$ , while all three parameters may be generally assumed in the case of Herschel-Bulkley fluids. Fig. 4c also shows two utilities for n and K determination in the case of power law fluids, that is, assuming Fann dial readings or viscosity and shear rate data are available.

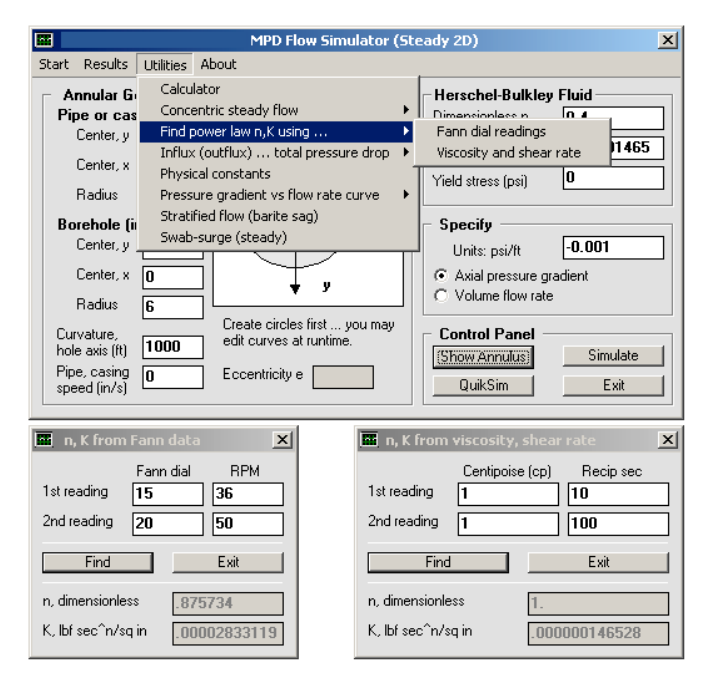


Fig. 4c - Determining n and K for power law fluids.

It is clear from Figs. 4a – 4c that several important auxiliary capabilities have been built into the overall algorithm. First, the axis of the borehole need not be straight; it may be curved, with any constant value for radius of curvature, to model short, medium and large radius turning of the borehole in offshore applications. This properly accounts for centrifugal effects which will affect the relationship between pressure gradient and volume flow rate.

Second, the drillpipe may move in either direction relative to the borehole, that is, constant speed translational motion is permitted. In the simplest application, the drillstring penetrates the formation, moves relative to the borehole at constant positive or negative speed, and induces a purely twodimensional flow everywhere; the value of this speed is entered into the bottom left input box of Fig. 4a. This capability also supports steady-state swab-surge analysis, with the mudpumps turned off or on and continuously running, as will be illustrated in examples later. A simple 'Worksheet' is loaded by clicking 'Swab-surge (steady)' in Fig. 4c, which prompts the user for tripping mode and speed. The positive or negative induced volume flow rate is calculated and added to the flow rate specified at the mud pump. Two calculation modes described in the next paragraph was developed for swab-surge and other drilling and cementing applications.

The option boxes immediately above the 'Control Panel' in Fig. 4a show how two computational modes are supported. In the first, the applied axial pressure gradient is specified and volume flow rate (together with detailed field solutions for all physical properties) is calculated. In the second, volume flow rate is specified and pressure gradient (together with all field properties again) is determined iteratively. The algorithm involves some subtlety because, as will be described in the application for swab-surge, the directions for drillpipe motion and net volume flow rate need not be correlated. For the "flow rate specified" mode, an initial pressure gradient is assumed for which a test rate is calculated and compared against the target rate; if the results do not satisfy a tolerance of 1%, a half-step correction procedure is applied to the test gradient and the calculations are repeated to convergence. Typically, the "pressure gradient specified" mode requires 2-3 seconds or less for a complete solution, while the "flow rate specified" mode may require up to ten seconds.

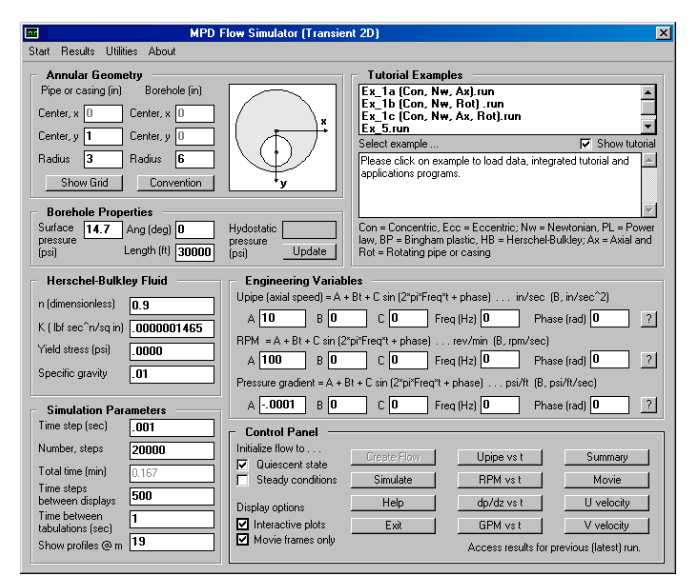


Fig. 4d - Transient flow user interface.

The foregoing remarks, focusing on the screen shot in Fig. 4a, apply to the steady flow simulator. The corresponding user interface for transient incompressible flow is shown in Fig. 4d. Now, instead of Eq. 4, fully unsteady effects are computed from its transient extension, but rewritten in custom curvilinear coordinates applicable to the particular geometry under consideration. The above menu contains similar geometry and rheology definition modules, however, general. coupled, transient functions for pipe or casing axial reciprocation, inner circle rotation and pressure gradient are permitted. Additional input boxes for time step selection to facilitate numerical time integration are shown. Importantly, a database of prior runs is offered for user convenience and education. Clicking on a named entry at the top right of Fig. 4d automatically fills in all relevant input boxes and launches any sub-applications programs that are required. Users may edit numerical values and re-run any simulations available in the database. Also, all graphical capabilities described in this paper for steady flow are also available for unsteady flows.

Color displays of engineering properties. In order to make the mathematical models useful, every effort was expended to automate the display of important field quantities using two and three-dimensional color graphics. Use of the presentation tools is completely transparent to the engineer. On convergence of the solution, a message box (supplemented with speech output and suggestions) summarizes basic pressure gradient and flow rate relationships.

The menu in Fig. 5a indicates that text output and color displays for different physical quantities are available for display. These quantities are post-processed from the velocity solution and made available for important engineering reasons. For example, Chin (1992, 2001) shows that apparent viscosity is vital to evaluating spotting fluid effectiveness in freeing stuck pipe. On the other hand, viscous stress (at the cuttings bed) is important to studying hole cleaning in horizontal and deviated wells, while velocity and viscosity play dominant roles in vertical well cuttings transport.

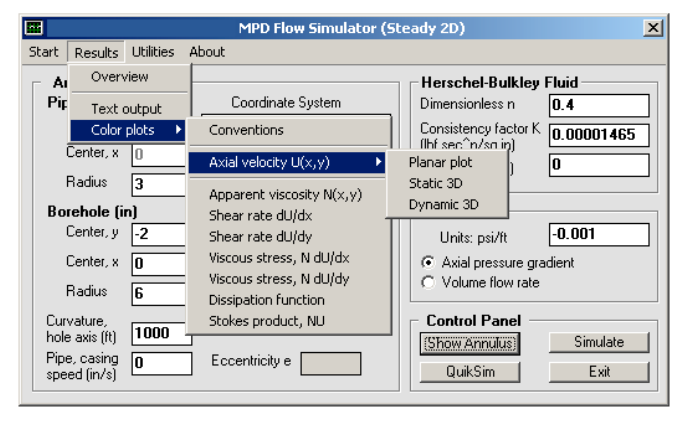


Fig. 5a - Graphical solution display options.

Fig. 5b displays results for axial velocity, apparent viscosity, shear rate, viscous stress, dissipation function and Stokes product in simple "planar plots." For the all-important velocity results, additional displays using three-dimensional

color capabilities are offered as indicated in Fig. 5c. These capabilities, which include contour plots and mouse-rotatable perspective displays, are available for all mesh combinations, ranging from coarse to fine, selected by the user at run-time. These tools, plus text output, are useful in supporting detailed report generation.

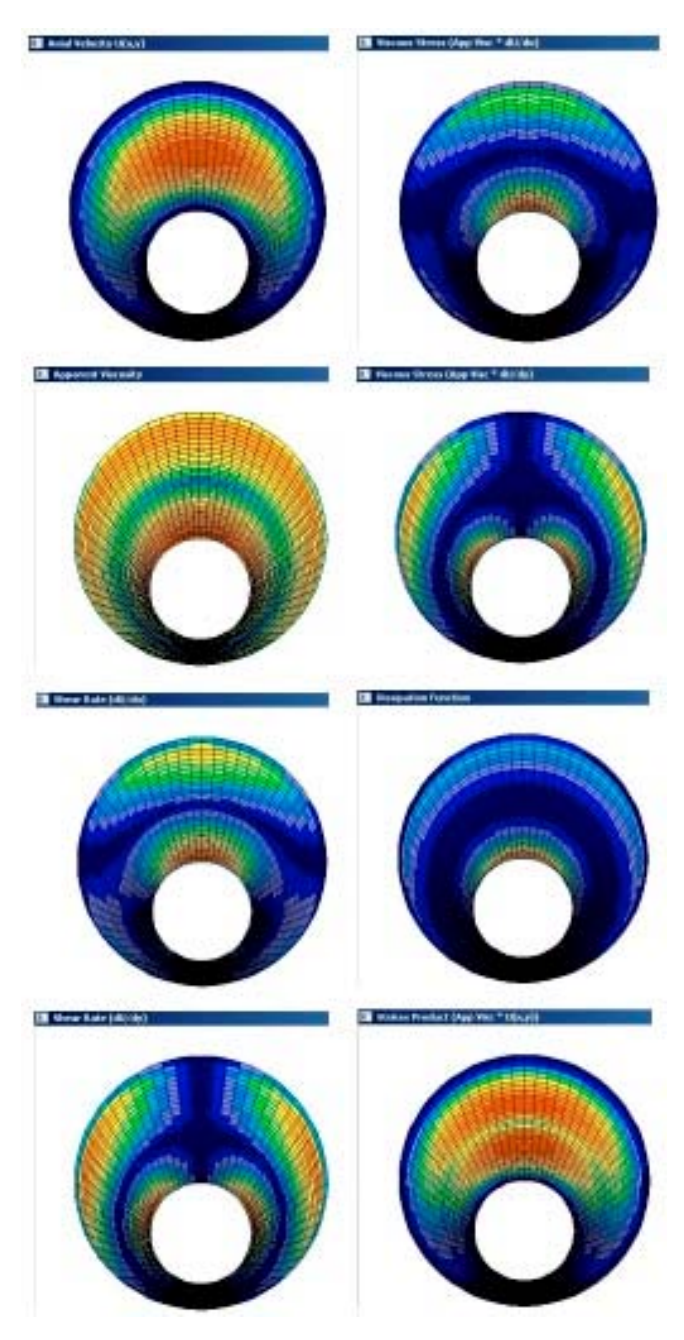


Fig. 5b - Planar color displays of key physical field quantities.

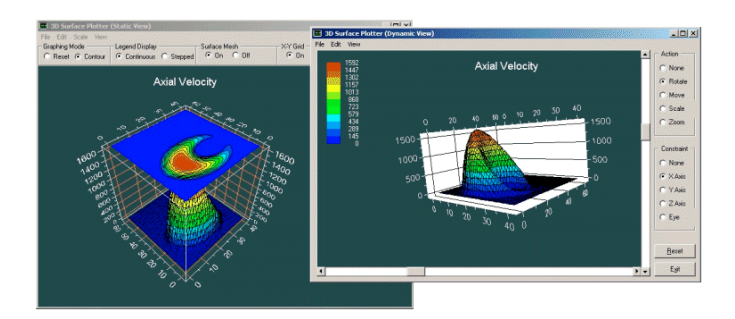


Fig. 5c – Three-dimensional, color displays (contour maps and mouse-rotatable perspective views).

Modeling borehole geometric irregularities. convenience, the main input screen in Fig. 4a accepts offcentered circles only. When center coordinates and radii are entered for inner and outer circles, an information box displays the calculated value for dimensionless eccentricity, to provide a useful reference point for drilling applications. Built-in error checking prevents circle cross-overs. At runtime, both inner and outer circle coordinates may be changed at the user's option. As shown in Fig. 6a below, existing contour coordinates are displayed, which may be modified without restriction. The changes elected for the example shown invoke changes to seven points only, in order to describe a simple washout; this convenient online editing tool can be used to draw washouts, cuttings beds and fracture indentations of any shape. While Fig. 6a provides a simple "planar plot" of velocity, Fig. 6b provides more detailed threedimensional resolution. Interestingly, for the simulation shown, the presence of the washout allows a 30% increase in flow rate for the same pressure gradient. General conclusions are not possible, and appropriate results must be made on a case-by-case basis.

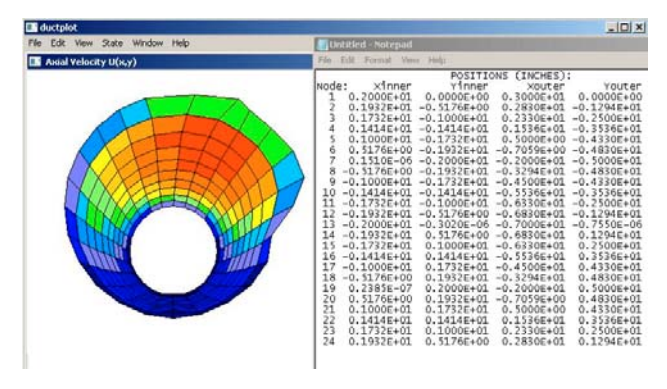


Fig. 6a - Modifying eccentric circle at run-time for washouts.

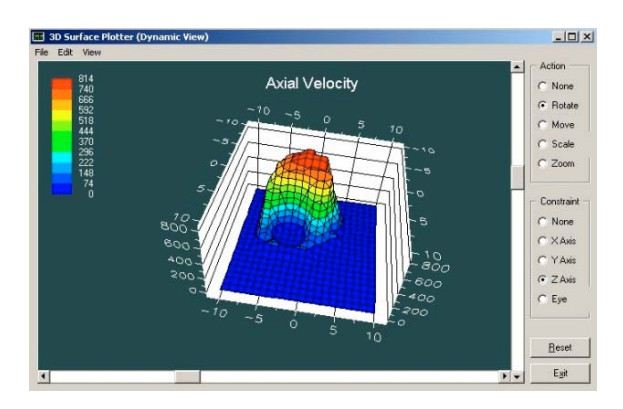


Fig. 6b - Color display of velocity field with washout.

**Yield stress modeling.** As noted earlier, yield stress modeling in eccentric annuli is important to both drilling and cementing applications. The use of the generalized Herschel-Bulkley constitutive model correctly predicts plug zone size and shape for all geometries. Because a continuous flow model is used, which guides the evolution of a single continuous velocity field, the computational difficulties associated with distinct internal boundaries and infinite viscosities are avoided. The method, we emphasize, will predict realistic plug zones with rapid gradients when they exist, as shown in Fig. 7a.

More interesting results are shown in Fig. 7b, in which plug zones for (1) a stationary pipe, (2) a pipe moving opposite to the direction of net flow, and (3) a pipe moving in the same direction of the main flow, are shown. Such computations are important in swab-surge applications and accurate pressure modeling. Plug zones associated with yield stress, of course, are important to understanding cuttings transport in drilling and fluid mixing in cementing. Again, no special procedures are required on the part of the user, as all dynamical features are computed automatically for both yield stress and non-yield fluids. Computation of plug zone flows requires no additional effort in terms of processing time and memory resources.

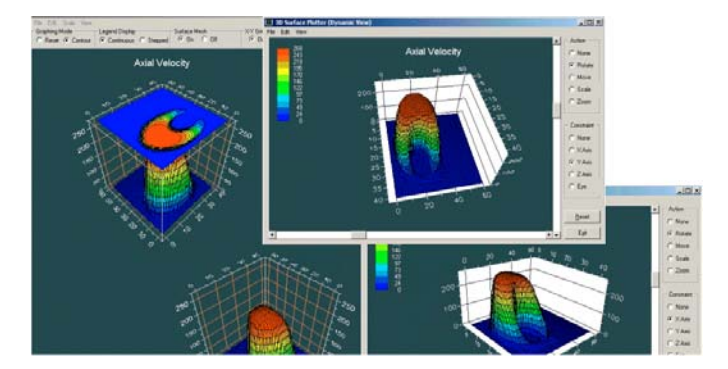


Fig. 7a – Typical velocity results for eccentric annulus with plug flow.

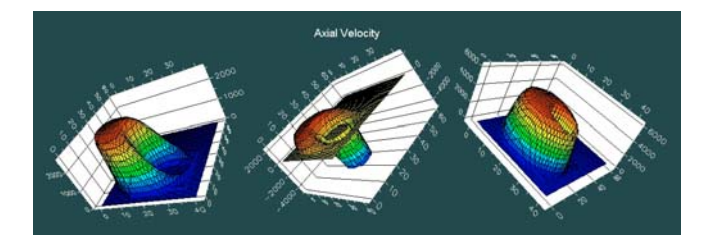


Fig. 7b – Non-Newtonian plug flow velocity profiles with stationary pipe (left), pipe moving opposite to flow (middle), and pipe moving with flow (right).

#### Overview - Detailed Eccentric Flow Results

The user interfaces in Fig. 4a and Fig. 4d, respectively, represent the "flagship simulators" for steady and transient flow modeling, both of which are directed at highly eccentric annular geometries containing yield stress fluids. We will give detailed calculated results in this section to demonstrate the new computational capabilities. However, we emphasize that a number of powerful "supporting simulators," also state-of-the-art, but hidden so far within the "Utilities" menus, are available for problems with more geometric restrictions.

Each detailed calculated example below is prefaced by introductory remarks indicating *why* the particular example is important. In the earlier discussion, we indicated that only seconds are required to compute and display results for general non-Newtonian flow in highly eccentric annuli. This assumes eccentric geometries constructed from off-centered circles, which are set up automatically by the software. If the hole contour is to be edited, e.g., to model washouts or cuttings beds, additional "desk time" requiring approximately five minutes is required. Then, as illustrated in Figs. 5a,b,c, all the details of the flowfield are known and automatically displayed in a simple manner to the user.

Chin (1992, 2001) importantly explains why different physical quantities are in practice important, supporting basic arguments with field and laboratory data. For instance, axial velocity and apparent viscosity are important parameters in vertical well cuttings transport; the argument follows the usual one explaining how hydrodynamic forces act on single particles immersed in flowing media. On the other hand, hole cleaning in horizontal and deviated wells depends on viscous stress at the top of cuttings beds, since viscous stresses effectively erode beds by mechanical action; this was illustrated using detailed data from University of Tulsa experiments. Apparent viscosity, for example, provides a good indicator for spotting fluid efficiency in freeing stuck pipe. The same reason for applying low viscosity oil to a nail stuck in wood (to remove it) holds here, and this simple explanation was also supported by Gulf of Mexico data.

**Preface to Example 4-8.** Prior to 2010, the calculation of steady eccentric annular flow when the inner pipe rotates with constant rpm proved to be a numerically unstable process. The instability was controlled by a parameter proportional to the product of fluid density and rotation rate and inversely proportional to apparent viscosity – calculations simply "crashed" and different explicit and implicit schemes

have been studied without success to remedy this problem. Unfortunately, the values yielding unconvergent results coincided with those parameters used in conventional drilling and cementing. Only two papers reported some optimism, but details related to formulation and computing times were not given. In this research, we encountered the same obstacles with purely steady formulations. On the other hand, it turned out that steady flows with rotation can be computed by performing transient calculations and allowing the time integrations to reach steady asymptotic values. Computing times, typically, are not long, with 1-3 minutes being average. Higher rotation rates and heavier fluids require shorter time steps, and computing times may reach five minutes. Short computing times are important so that the software model is useful in actual practice. Example 4-8 below provides a series of runs obtained using the simulator of Fig. 4d. These applications include axial movement, pipe movement and yield stress.

## Example 4-8. Steady-state swab-surge in eccentric annuli for Herschel-Bulkley fluids with drillpipe rotation and axial movement.

In Example 4-7, we addressed pressure gradient computations for general flow rates and rotation speeds for power law fluids in a concentric annulus under steady conditions without axial pipe movement. For such flows, the convective terms in the momentum equations vanish identically. The effect of rotation is restricted to shearthinning so that, for a given pressure gradient, increases in rotation rate will reduce apparent viscosity and increase volumetric flow. These effects are well known in the older literature and apply mainly to vertical wells.

Run A. In deviated and horizontal wells, annular eccentricity is the rule, and while shear-thinning remains important, a nonlinear convective term (whose magnitude is proportional to fluid density and pipe rotation speed and inversely proportional to apparent viscosity, and which is variable throughout the annular cross-section) appears and modifies the local axial pressure gradient. For most practical geometries, this will reduce the flow relative to that found for the eccentric non-rotating problem for the same applied pressure gradient. Equivalently, for the same flow rate, the pressure drop increases significantly. These properties are important in managed pressure drilling.

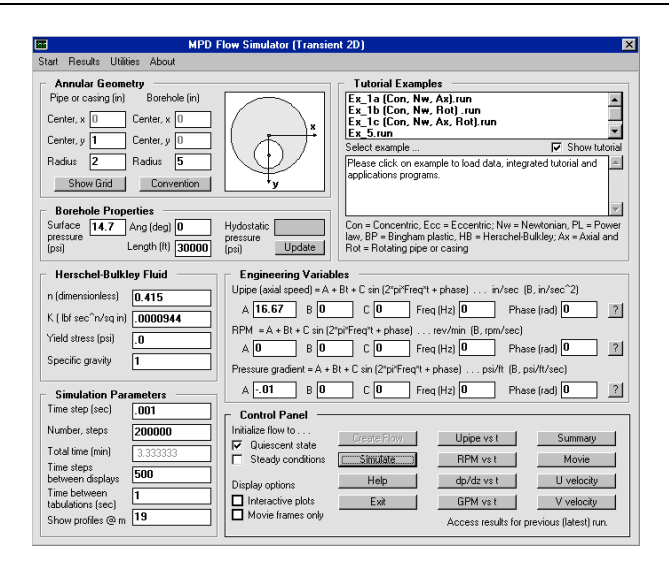


Fig. 4-8a-1 - Transient 2D flow menu (no rotation).

The direct computation of steady rotating flow in an eccentric annulus is often an unstable numerical process if calculated from a purely steady formulation. Solutions have been published by various authors who have all given few computational details related to convergence properties and computing times. Such schemes tend to destabilize at higher specific gravities and rotation speeds, and unfortunately, in the ranges typical of most drilling applications. Fortunately, steady rotating flow solutions can be stably computed by solving the transient formulation asymptotically for large times. In Fig. 4-8a-1, we have set up flow simulations for a power law fluid in an eccentric annulus with axial pipe movement but no rotation. The problem is integrated in time starting with quiescent conditions. Fig. 4-8a-2 shows computed volume flow rates reaching constant levels at 941.0 gpm after about one minute of computing time (this is interestingly, but fortuitously, also the physical time scale) with convergence to steady-state achieved very stably. The maximum axial flow speed is found, as expected, at the wide side of the annulus.

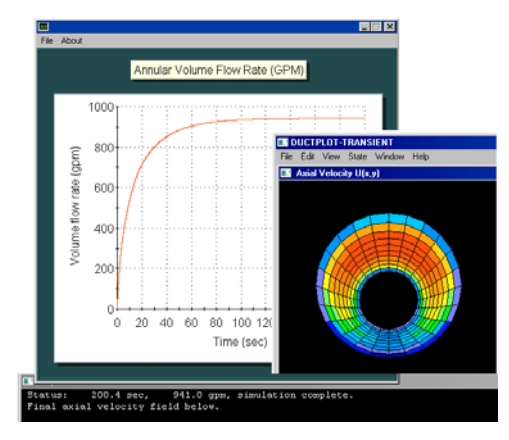


Fig. 4-8a-2 - Eccentric power law results without pipe rotation.

Run B. Repeating the foregoing simulation to allow drillstring rotation is straightforward. For example, we simply change the "0" in the RPM box to "100" (as seen from Fig. 4-8b-1) and completely automated calculations lead to a reduced flow rate of 562.2 gpm as shown in Fig. 4-8b-2. As is well known, the location of maximum axial velocity moves azimuthally, and the results are consistent with this observation, a fact that may be useful in cuttings transport and hole cleaning applications. Computed results also indicate that the time to reach equilibrium decreases with rotation. The results presented here, for pipe moving both axially and azimuthally, show that pressure gradient calculations are doable and straightforwardly performed for general power law fluids in highly eccentric annuli.

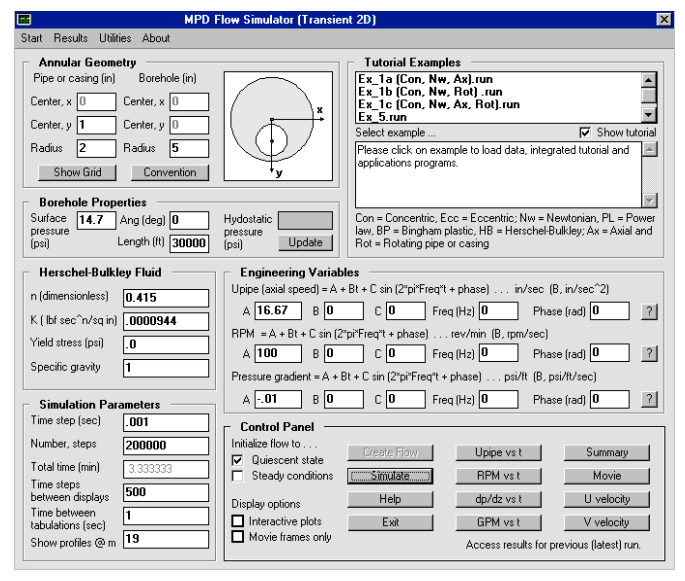


Fig. 4-8b-1 - Modified flow with 100 rpm drillstring rotation.

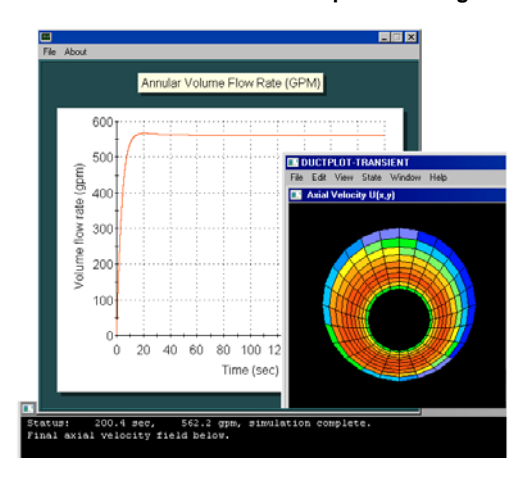


Fig. 4-8b-2 – Reduced flow rate achieved in shorter time.

**Run C.** In the next calculation, we repeat that in Fig. 4-8b-1, which included axial pipe movement and nonzero rotation speed in addition to borehole eccentricity and non-Newtonian power law flow, but now consider the additive effects of Herschel-Bulkley yield stress. In Fig. 4-8c-1, we

modify the previous "0" to "0.002 psi" and leave all other parameters unchanged. As before, the calculations require about 30 seconds and are performed stably.

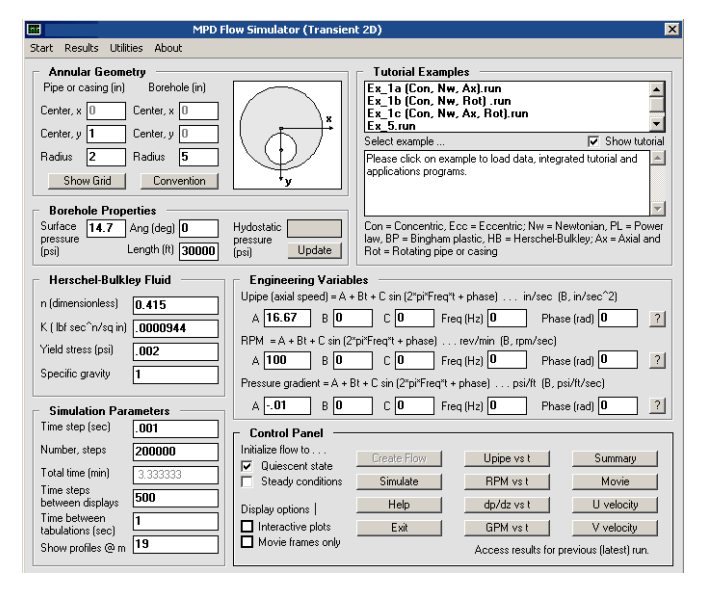


Fig. 4-8c-1 - Flow at 100 rpm now with 0.002 psi yield stress.

Fig. 4-8c-2 shows that the volume flow rate is reduced from 562.2 gpm to 516.9 gpm, for a 9% reduction. One might have asked what the required pressure gradient would be for the yield stress fluid if we needed to maintain a 562 gpm flow rate. For the steady flow solver, direct "pressure gradient specified" and inverse "flow rate specified" calculation modes were available. For mathematical reasons, this is not practical for transient simulations. A simple procedure requires us to manually attempt reasonable pressure gradient guesses. This procedure can be very efficient. For this example, we determined that – 0.011 psi/ft would yield 562 gpm after three tries or about two minutes of desk time. In other words, the presence of yield stress steepened the pressure gradient by a substantial 10%.

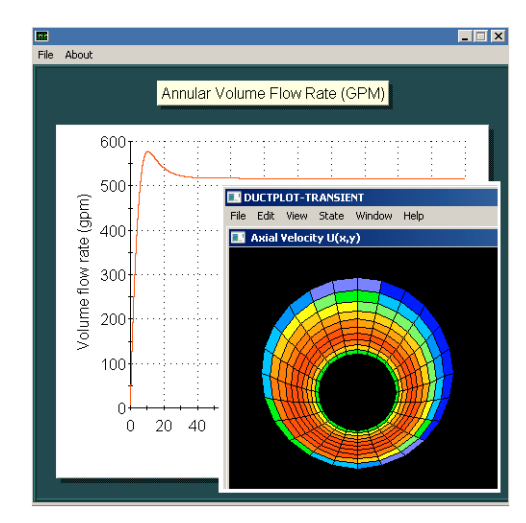


Fig. 4-8c-2 - Flow at 100 rpm now with 0.002 psi yield stress.

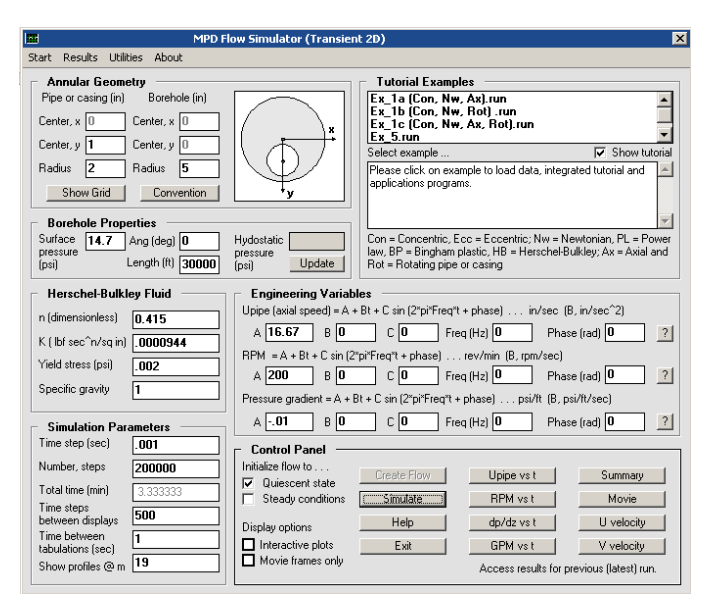


Fig. 4-8d-1 - Flow at 200 rpm with 0.002 psi yield stress.

**Run D.** Next, we will re-consider the yield stress problem in Fig. 4-8c-1 and determine the consequences of increasing rotation rate from 100 to 200 rpm. The input screen is shown in Fig. 4-8d-1. The effect of doubling rotation speed is a decreased flow rate for the same – 0.01 psi/ft, in this case a much smaller 443.3 gpm, as shown in Fig. 4-8d-2. This effect arises from eccentricity. And what if we had insisted on 562 gpm? Then, some simple manual "cut and try" calculations with different pressure gradient guesses lead to a substantially steepened – 0.0131 psi/ft, a value that was obtained within two minutes with four different guesses.

Favorable effect of rotation on hole cleaning. The detailed effects of rotation and yield stress have been discussed in the context of eccentric borehole annuli with coupled axial drillstring movement. These calculations represent completely new industry capabilities. interesting to note that, from Fig. 4-8a-2 for non-rotating flow, the location of maximum axial flow speed lies symmetrically at the top at the wide side of the eccentric annulus. When rotation exists, as shown in Figures 4-8b-2, 4-8c-2 and 4-8d-2, the location of the maximum moves azimuthally as shown, consistently with other known investigations (note that "red" in these three diagrams denote different speeds). increased relative speeds are achieved at the bottom of the annulus is consistent with the improved hole cleaning ability of drillstrings under rotation observed under many field conditions. Of course, this improvement comes at the expense of steepened pressure gradients, a crucial trade-off whose value must be assessed by the drilling engineer. The end decision made at the rigsite will depend on "the numbers" which can only be obtained computationally.

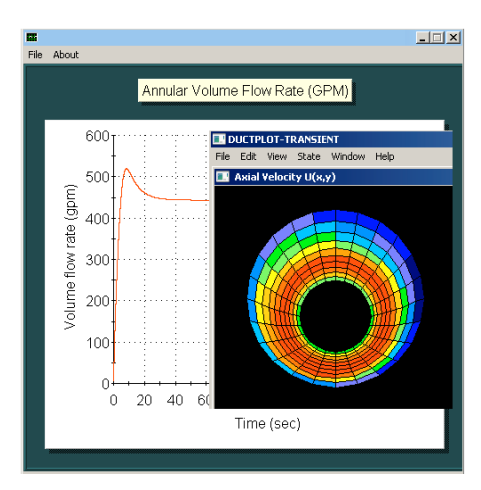


Fig. 4-8d-2 - Flow at 200 rpm with 0.002 psi yield stress.

Here we study the effect of slow-down in drillstring rotation rate (the menus support more complicated motions, e.g., stick-slip torsional oscillations). Acceleration and deceleration are always encountered in start-up and slowdown. We repeat the calculation of Fig. 4-8d-1, starting with 200 rpm for the nonzero yield stress fluid. But as shown in Fig. 4-8e-1, we allow the 200 rpm to slow down to 0, as seen from the "- 0.5" deceleration rate selected under the RPM menu. Clicking on "?" to the right produces a plot of the assumed RPM vs time curve in Fig. 4-8e-2 (note that numerous time functions for axial pipe speed, rotation rate and pressure gradient are permissible with the simulator). The calculated flow rate vs time response is shown in Fig. 4-8e-3. This flow rate increases as expected, with drillstring rotation rate decreasing. In this transient simulation, the location of maximum axial velocity is not stationary, but instead propagates azimuthally about the eccentric annulus. "snapshot" at one instant in time is shown in Fig. 4-8e-4. Although this example is purely transient, we have included it in the steady eccentric annular flow example to highlight the importance (or perhaps, unpredictability) of transient effects. The shape of the transient rate curve in Fig. 4-8e-3, we emphasize, is obtained for a simple Herschel-Bulkley fluid and not one with "memory" effects.

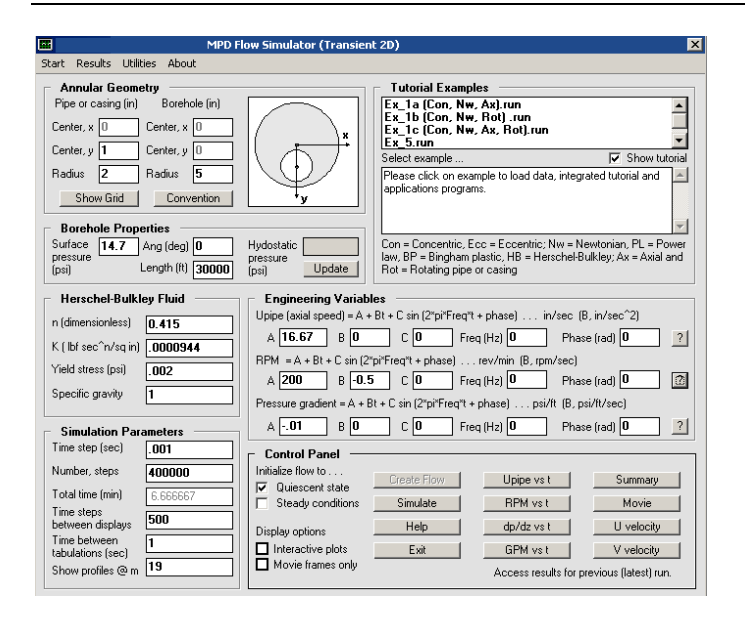


Fig. 4-8e-1 - Decreasing rotation rate, from 200 to 0 rpm.

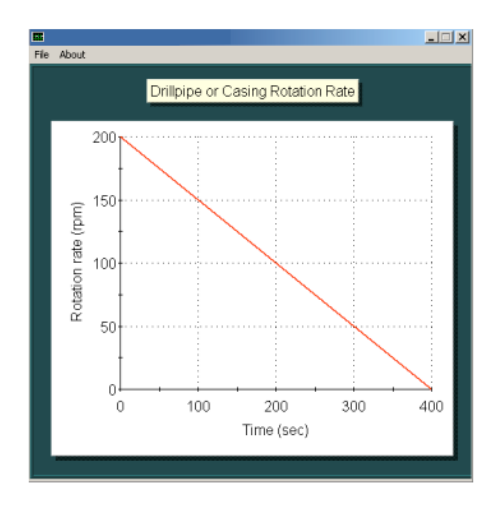


Fig. 4-8e-2 - Linearly decreasing rpm, from 200 to 0.

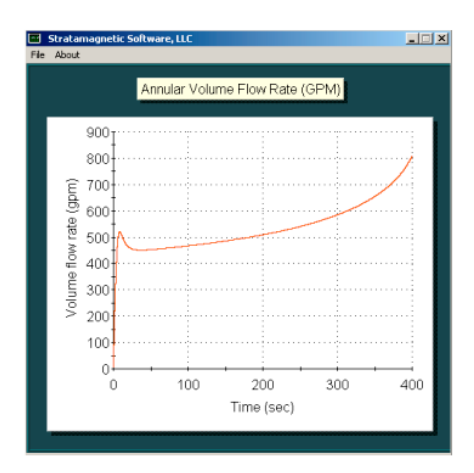


Fig. 4-8e-3 – Transient increasing flow rate with decreasing rpm.

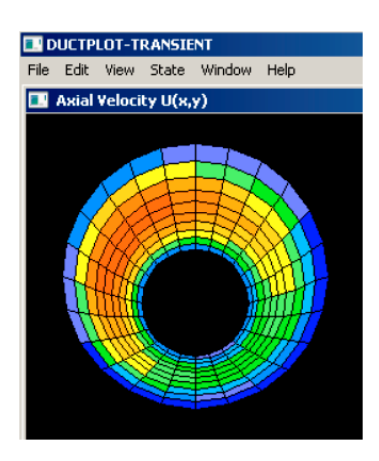


Fig. 4-8e-4 – Transient movement of maximum point as rpm decreases.

Run F. In this final example, we consider a complete steady swab-surge application with high annular eccentricity, a nonlinear yield stress fluid, and allow the drillpipe to move axially while simultaneously rotating. This demonstrates the capabilities in the math models and provides a complete summary of the software menu sequences needed to perform similar calculations. In order to proceed, the "Swab-Surge Worksheet" must be invoked from the main "MPD Flow Simulator (Steady 2D)" in Fig. 4-8f-1. In the Worksheet, we consider a five-inch radius hole and a pipe trip-out speed of 5,000 ft/hr. During this operation, we wish to pump continuously, with the surface mudpump rate set at 856.9 gpm. Now, as the drillpipe is withdrawn from the hole, fluid must rush in to fill the bottomhole void. The Worksheet indicates that the effective annular flow rate is 516.9 gpm and that the pipe speed in "inch/sec" units is 16.67 in/sec.

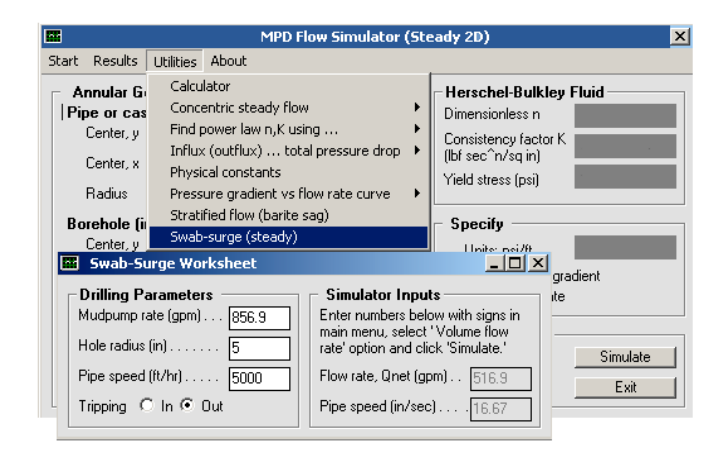


Fig. 4-8f-1 – Running the "Swab-Surge Worksheet" (areas that do not affect Worksheet calculator are shown shaded).

Now, we wish to focus the study on the non-Newtonian flow of a Herschel-Bulkley fluid with n=0.415, K=0.0000944 lbf  $sec^n/in^2$  and  $\tau_0=0.002$  psi, in an annulus formed by a 4 in diameter pipe in a 10 inch diameter hole, with an eccentricity of 0.3333. We will demonstrate the solution process for flows without and with rotation. If we

wish to consider axial movement only but without rotation, we can run the steady flow calculation shown in Fig. 4-8f-2 in "volume flow rate specified" mode. Clicking on "QuikSim" produces the screen output iteration history shown on the following page.

```
SIMULATION STARTS ..
Herschel-Bulkley model, with exponent "n" equal
to 0.4150E+00 and consistency factor of 0.9440E-04
lbf sec^n/sq in.
A yield stress of 0.2000E-02 psi is taken.
Borehole axis radius of curvature is 0.1000E+04 ft.
Axial speed of inner pipe is 0.1667E+02 in/sec.
Target flow rate of 0.5169E+03 gal/min specified.
Iterating on pressure gradient to match flow rate ...
Iteration
           100, Error = .00672962
Iteration
           200, Error =
                        .00248959
                        .00119476
Iteration
           300, Error =
Iteration
           400, Error =
                        .00052236
Iteration
           500, Error =
                        .00019270
Iteration
           600, Error =
                        .00005923
Iteration
           700, Error =
                        .00001814
Iteration
           800, Error =
                        .00000521
Iteration
           900, Error =
                        .00000171
Iteration 1000, Error = .00000047
  Axial pressure gradient of -.1000E+00 psi/ft
   yields volume flow rate of 0.4076E+06 gal/min.
Flow rate target error is 0.7876E+05 %
           100, Error = .00371665
Iteration
Iteration
           200, Error =
                        .00067117
Iteration
           300, Error =
                        .00014123
Iteration
           400, Error =
Iteration
           500, Error =
                        .00000702
Iteration
           600, Error =
                        .00000192
Iteration
           700, Error =
                        .00000038
Iteration
           800, Error =
                        .00000010
Iteration
          900, Error = .00000010
Iteration 1000, Error = .00000010
  Axial pressure gradient of -.5000E-01 psi/ft
   vields volume flow rate of 0.4141E+05 gal/min.
Flow rate target error is 0.7911E+04 %
  Axial pressure gradient of -.6250E-02 psi/ft
   yields volume flow rate of 0.6708E+03 gal/min.
Flow rate target error is 0.2977E+02 %
Iteration 100, Error = .00000000
           200, Error = .00000011
Iteration
Iteration
           300, Error = .00000000
                        .00000011
Iteration
           400. Error =
                        .00000011
Iteration
           500, Error =
Iteration
           600, Error =
                        .00000011
                        .00000000
Iteration
           700, Error =
Iteration
           800, Error = .00000021
Iteration
           900, Error = .00000011
Iteration 1000, Error = .00000000
  Axial pressure gradient of -.4688E-02 psi/ft
   yields volume flow rate of 0.5217E+03 gal/min.
```

gradient

found

vield 0.5217E+03 gal/min vs target 0.5169E+03

Note: Iterations terminate within 1% of target rate. Refine result by manually changing pressure gradient.

iteratively,

Pressure

to gal/min.

psi/ft,

- 4688E-02

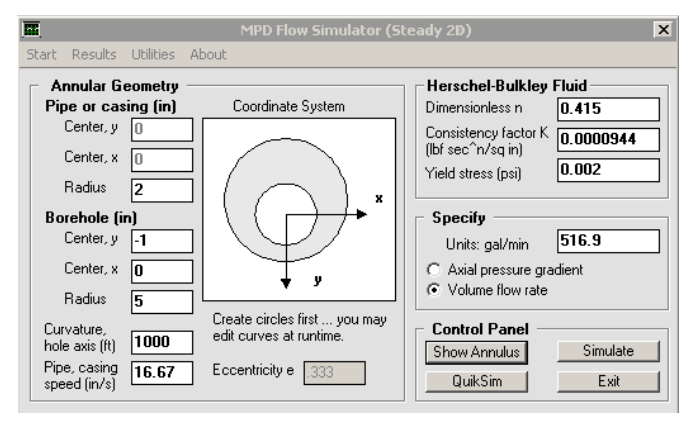
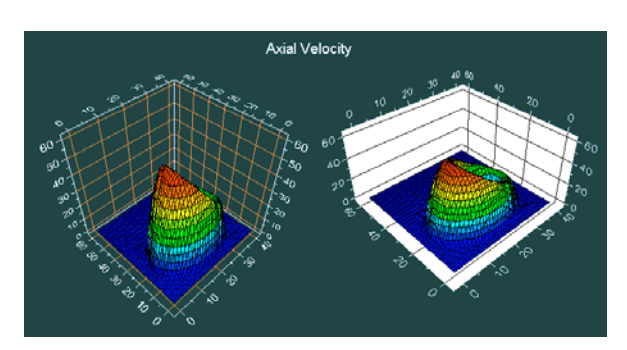


Fig. 4-8f-2 - Steady 2D solver.



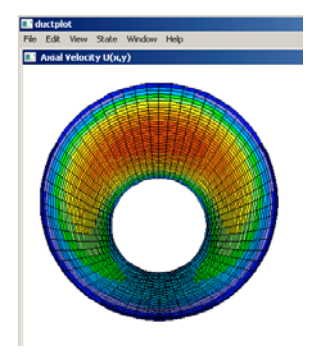


Fig. 4-8f-3 - Computed axial velocity (non-rotating).

In other words, the pressure gradient associated with the non-rotating flow is - .004688 psi/ft. The corresponding axial velocity field is shown in Fig. 4-8f-3 in a variety of available plots. Note that for non-rotating flows, the "Steady 2D" solver automatically computes the required pressure gradient using an internal inverse procedure. It has not been possible to develop a steady solver that allows rotation which is also unconditionally numerically stable. This does not, fortunately, mean that steady rotating flows cannot be computed.

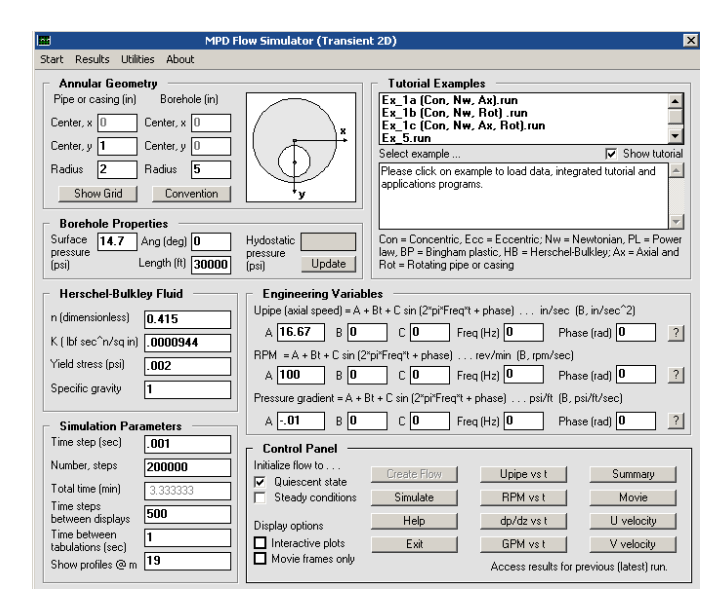


Fig. 4-8f-4 - Transient 2D solver.

We demonstrate how by considering the effect of a moderate 100 rpm rotation rate. We use the "Transient 2D" solver in Fig. 4-8f-4, with input boxes completed for the same simulation parameters. The strategy is to solve a fully transient problem until steady-state behavior is obtained. Because a "flow rate specified" mode is not available for transient calculations, one resorts to repeated guesses for pressure gradient, but we have found that three or four will usually lead to a flow rate within 1-2% of the target value. Since each trial calculation equilibrates quite rapidly, as shown in Fig. 4-8f-5, the total "desk time" required is often two minutes or less.

For this rotating flow run, a pressure gradient of -0.01 psi/ft is required, as compared to the -.004688 psi/ft obtained in the non-rotating case. In other words, pressure gradients are twice as severe because of rotation. The "Results" menu in Fig. 4-8f-4 provides numerous post-processed results in addition to those of Fig. 4-8f-5. For example, axial and azimuthal velocity distributions are available, as given in Fig. 4-8f-6, as are detailed color plots of different physical properties like apparent viscosity, shear rate and viscous stress.

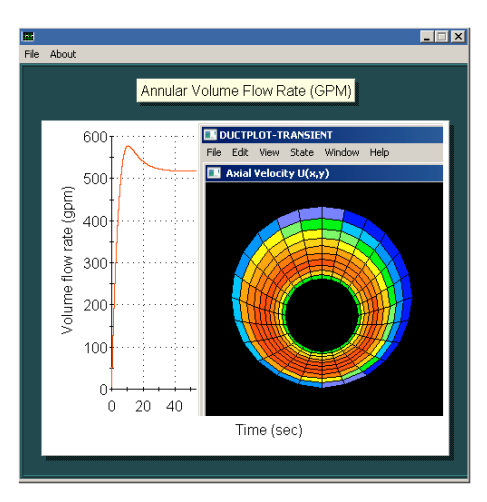


Fig. 4-8f-5 – Flow rate history and velocity distribution (note, maximum axial velocities appear at annular bottom).

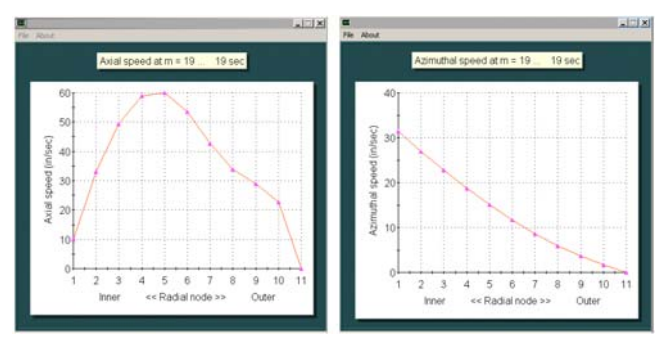


Fig. 4-8f-6 – Axial and azimuthal velocities at cross-section "m = 19."

**Preface to rotating flow examples.** The modeling of rotating flow effects using a transient approach involved much more than simply adding a " $\rho \partial u/\partial t$ " to Eq. 4 (for steady flow) and integrating the unsteady equation in time. Numerous questions have arisen in the petroleum engineering literature about the effects of rotation on pressure drop or flow rate, and it was not clear if any of the inconsistencies and controversies could even be explained by a simple mathematical model. Moreover, numerical solutions introduce their own artifacts. For instance, the way a function is approximated over several grid points affects the way in which it contributes "artificial viscosity" to the scheme. This interacts with the rheological model used, and needless to say, numerous issues arise.

The basic problem in rotating flow applications is summarized. In pre-1990s literature, exact non-Newtonian flow solutions and field experiences consistently demonstrated that drillstring rotation increases flowrate for a fixed pressure gradient, or equivalently, decreases pressure gradient (magnitude) for a fixed flowrate, the effect being attributed to apparent viscosity reduction due to shear-thinning. Field experiences in the past two decades, however, indicate the exact opposite, and recent papers have failed to determine the causes of the apparent contradictions and resulting confusion. It turns out that there are no inconsistencies: the boreholes considered recently are highly eccentric because they are

deviated or horizontal, for which new convective terms in the governing momentum equations appear which are due to annular eccentricity and which modify the effective pressure gradient (these terms are not present in older studies, which consider only concentric annuli). Exact numerical solutions demonstrate the role of eccentricity in changing flowrate or pressure gradient during drilling. Because the changes are not small, drillstring rotation can be used to control pressure in managed pressure drilling applications and in cementing. The implications are more efficient drilling and improved safety. The computational model developed uses boundaryconforming, curvilinear mesh systems to describe annular geometry exactly, and rapidly converging, stable, transient algorithms have been developed to solve the general rheology equations with and without yield stresses. It can be shown from theoretical arguments that -

- In Newtonian flow, the viscosity is a constant of the motion (barring changes due to pressure and temperature) which is unambiguously determined from viscometer measurement.
- In non-rotating Newtonian flow, the lumped quantity (1/µ) ∂p/∂z controls the dynamics, and changes to it will proportionally change u(y,z) everywhere thus, faster testing with inexpensive fluids, together with simple arithmetic extrapolation, can be used in engineering design.
- For concentric annuli in steady Newtonian rotating flow, azimuthal velocities do not depend on pressure gradient, and axial flows are unaffected by rotation: the two are dynamically uncoupled.
- Annular eccentricity introduces changes to the applied pressure gradient that are variable throughout the flow domain (the velocity likewise scales differently at different cross-sectional locations) when rotation is allowed. Their magnitudes are proportional to the product "density × rpm / viscosity." This effect generally decreases the flow rate (as rotation speed increases) for a fixed pressure gradient this nontrivial modification applies even to simple Newtonian fluids without shearthinning.
- Non-Newtonian fluids (even without rotation and three-dimensionality) exhibit shear-thickening and shear-thinning properties. In a concentric annulus with a rotating inner pipe, drilling fluid viscosity will decrease due to azimuthal motion so that net flow rate increases relative to the non-rotating case assuming that pressure gradient is fixed. Complications arise when this is countered by the effects of eccentricity computational methods are required to determine the exact balances between the two.
- Non-Newtonian flows in eccentric borehole annuli with rotation will exhibit shear-dependent changes to viscosity, plus changes to applied pressure gradient that depend on

- rotation speed, fluid density and viscosity (the "apparent viscosity" now varies throughout the flow domain). Simple rescaling arguments cannot be used to deduce flow properties for u(y,z) because the governing equations are extremely complicated in form.
- For non-Newtonian flows, laboratory testing and extrapolation is not possible because of the foregoing complications – hence, the only recourse for prediction and job planning is full-scale testing with actual nonlinear fluids or, alternatively, detailed computational fluiddynamics analysis.

### Example 7-6. Effect of steady rotation for power law flows in highly eccentric annuli at low densities (foams).

In this example, we examine a cross-section with high eccentricity and also allow for nonlinear power law fluid motion. Here, the eccentricity is 0.5. Results for a nonrotating pipe are given in Figure 7-6a, where a steady flow rate of 1,052 gpm is indicated. The time required to achieve steady-state is approximately one second. What happens if we rotate the drillpipe at 300 rpm? Figure 7-6b shows that with rotation, the time to reach steady conditions is reduced; also, the flow rate decreases to 905.8 gpm. This suggests that in the complementary problem when volume flow rate is fixed, the effect of rotation is to increase (the absolute value of) pressure gradient. Consistent with the previous example, the decrease in flow rate occurs because of inertia effects. We emphasize that the flow rate reduction due to rotation seen here is a Finally, in Figure 7-6c, we re-run the sizeable 16%. simulation with the initial fluid assumed to be non-rotating and flowing. The results show an equilibration time of one second between steady states so that flow changes are sudden and dangerous. The steady-state flow rate is again about 900 gpm. There is a "bump" in the gpm vs time curve, one seen repeatedly in many such simulations. Whether or not this effect is real will require laboratory observation. All of the calculations for this example were performed stably, as the line graphs show, and required only 2-3 seconds of computing time.

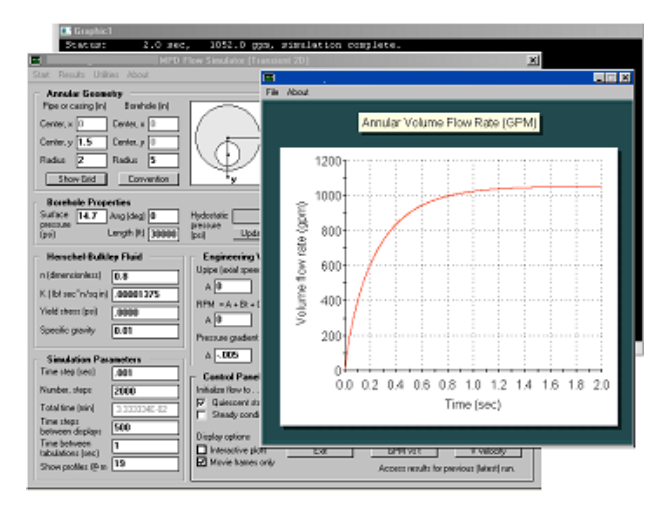
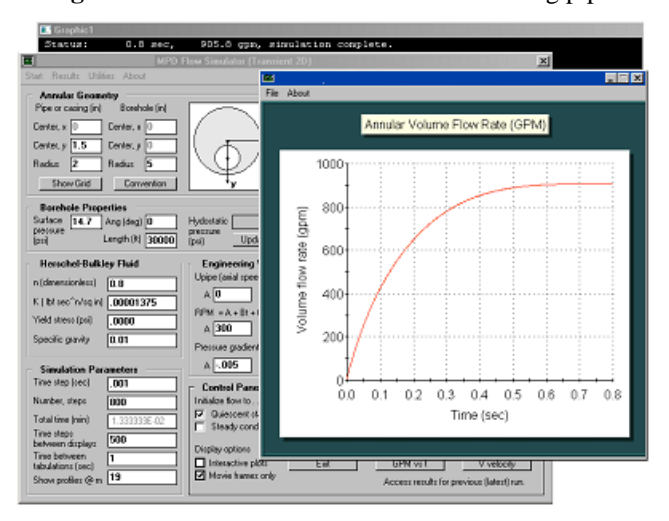
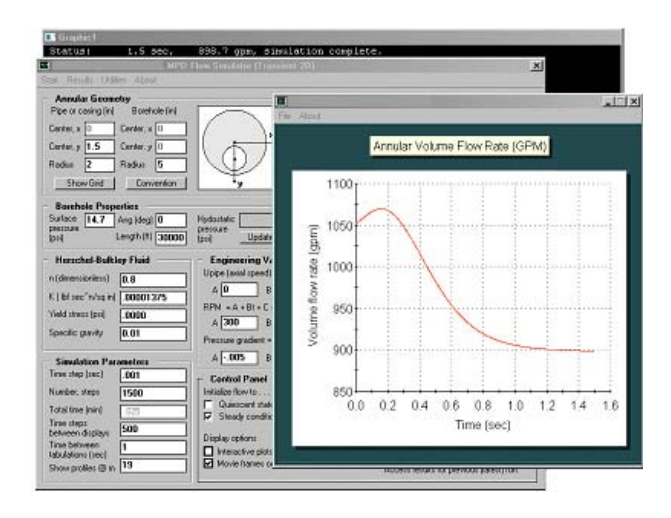


Figure 7-6a. Power law flow with non-rotating pipe.



**Figure 7-6b.** Power law flow with rotating pipe (zero starting conditions).



**Figure 7-6c.** Power law flow with rotating pipe (from flowing conditions).

It is important to point out some important software details associated with flow initialization. For steady flow formulations, the initial state of the flow does not appear as a parameter because there is no variation in time (actually, it does in a numerical sense, since initial solution guesses are taken, although internally to the software). For transient formulations, the initial state must be specified. If quiescent stagnant-flow conditions are selected, the box shown in Figure 7-6d is checked and "Simulate" can be clicked immediately.

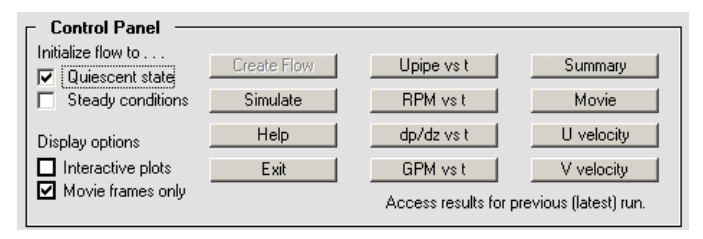


**Figure 7-6d.** Assuming quiescent, stagnant-flow initial conditions.

On the other hand, the fluid may be moving initially at t=0, and *then*, the transient flow specifications shown in the user interface is applied. If the initial flow is not rotating, we know that its solution does not depend on density; we can therefore calculate it assuming a very small value of  $\rho$  together with large time steps. If we wish to initialize to a non-rotating steady flow, the message box in Figure 7-6e appears, reminding the user to click "Create Flow" to start this process. Once this is completed, the "Simulate" button can be clicked to perform the required transient analysis.

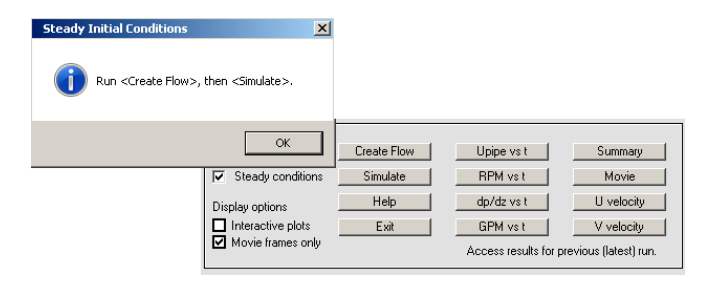


**Figure 7-6e.** Creating a non-rotating, steady initial flow.

If the starting flow is rotating, its solution does depend on density and time steps will need to be very small to ensure convergence. This initialization is not supported at the present time because the solution procedure cannot be made as robust or automatic as desired, but continuing research is being pursued in this area.

## Example 7-7. Effect of steady rotation for power law flows in highly eccentric annuli at high densities (heavy muds).

We emphasized earlier that for non-rotating flows, the effects of density vanish at large times. Thus, in computing non-rotating steady-state flows with the transient algorithm, it is advantageous to use as small a fluid density as possible in order to quickly converge the calculations. Here we wish to evaluate the effects of mud weight under rotating conditions. For the non-Newtonian eccentric flow in Figure 7-7a, a very low specific gravity of 0.01 leads to a flow rate of 898.5 gpm. Next we wish to consider the opposite extreme, e.g., a heavy mud or cement with a specific gravity of two. Because the unstable convective term never vanishes when the pipe rotates (its magnitude is proportional to fluid density and pipe rpm), we decrease the time step to 0.0001 sec and increase the number of time steps simulated. The resulting flow rate is a much lower 135.1 gpm. Computation times for the two runs are five seconds and two minutes, approximately. Finally, we reduce the specific gravity to 1.0, i.e., an unweighted mud. Will the flow rate vary linearly with density, that is, fall midway between 135.1 and 898.5 gpm? Figure 7-7c shows that the flow rate is, in fact, 160.1 gpm. This unpredictability shows why computer models are important to real-world field job planning.

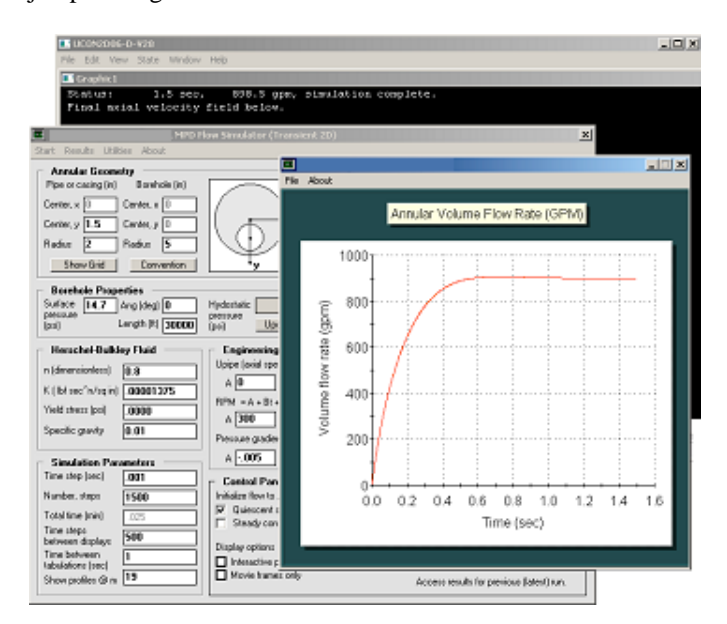


**Figure 7-7a.** Very low density fluid (e.g., foam) at high rpm.

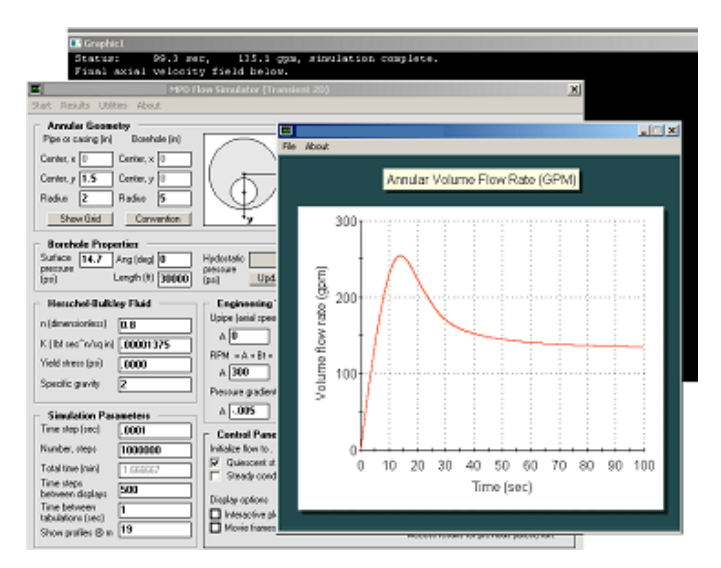


**Figure 7-7b.** Very high density fluid (e.g., heavy mud or cement) at high rpm.

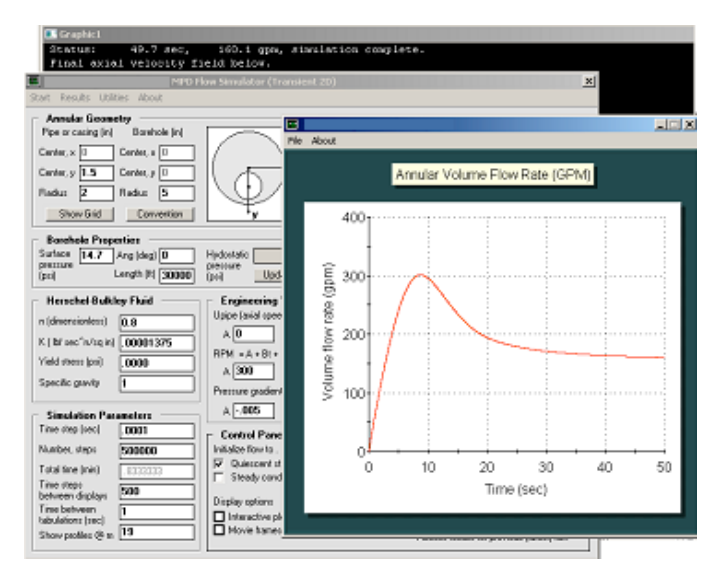


**Figure 7-7c.** Unweighted fluid (e.g., water or brine) at high rpm.

### Example 7-8. Effect of mudpump ramp-up and ramp down flowrate under non-rotating and rotating conditions.

In Figure 7-8a, we consider a power law fluid in an eccentric annulus under a constant imposed pressure gradient of -0.005 psi/ft with the drillpipe completely stationary. This is seen to produce a steady-state flow rate of 1,051.8 gpm as shown. In practice, the mud pump starts and stops, and transient effects are associated with ramp-up and ramp-down. We ask, "How are pressure gradient and flow rate transient properties related?"

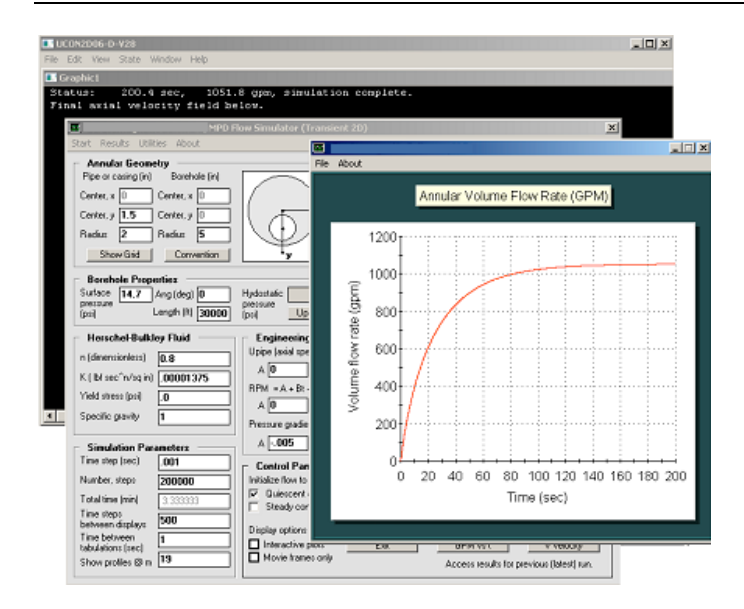
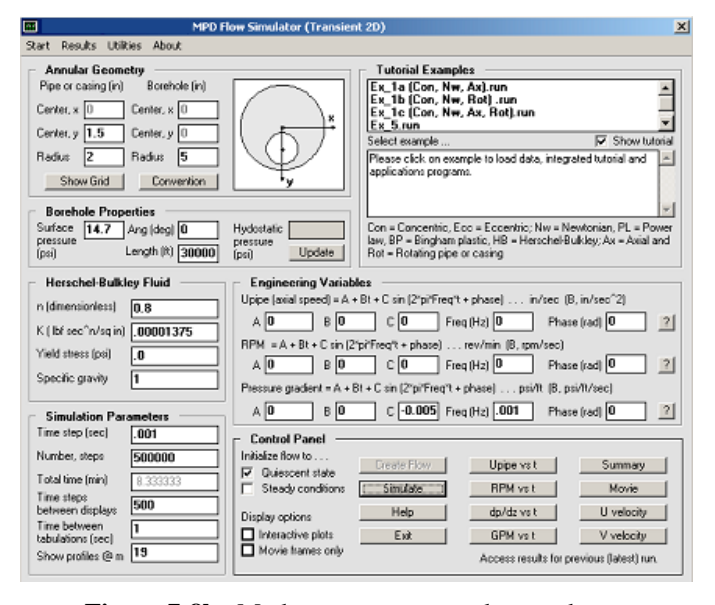
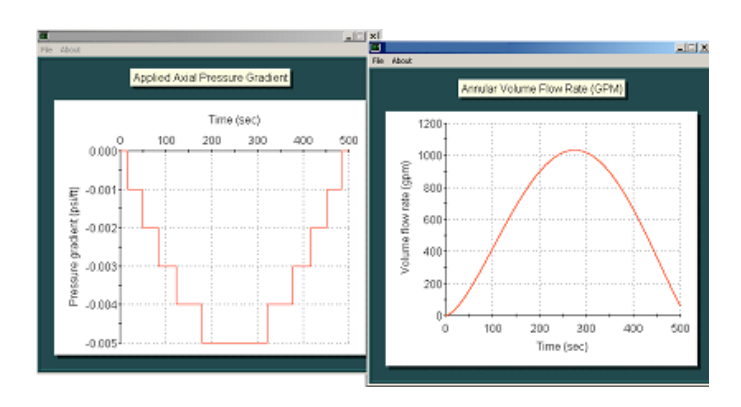


Figure 7-8a. Constant pressure gradient calculation.

To answer this question, we modify several menu entries of Figure 7-8a so that the pressure gradient is no longer constant. The assumption shown in Figure 7-8b allows a sinusoidal ramp-up from quiet conditions to the previous value of -0.005 psi/ft, followed by a full ramp-down. This is accompanied by time mesh refinement plus the use of additional time steps. Clicking on the "?" to the far right of the pressure gradient menu produces the left-side diagram of Figure 7-8c showing pressure assumptions. The right-side diagram gives the computed volume flow rate as a function of time.



**Figure 7-8b.** Mudpump ramp-up and ramp-down.



**Figure 7-8c.** Assumed pressure gradient and calculated flow rate.

Next, we determine the effect of drillstring rotation. We simply change the zero rotation input in Figure 7-8b to allow for a 100 rpm rotation rate as shown in Figure 7-8d. For the same pressure gradient variation as above, the flow rate is now substantially reduced as shown in Figure 7-8e.

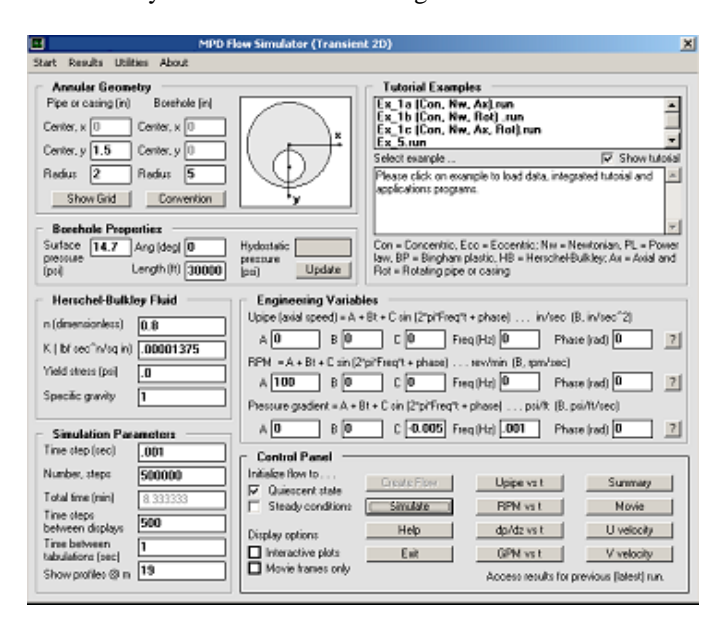


**Figure 7-8d.** Increasing rotation rate to 100 rpm.

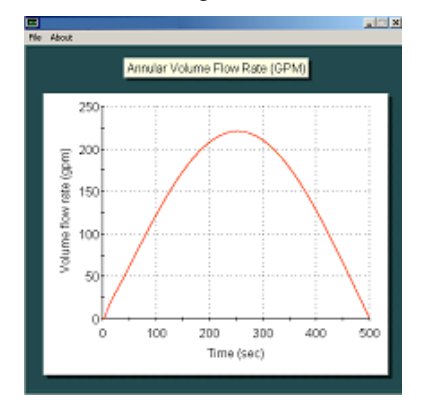


**Figure 7-8e.** Significantly reduced volume flow rate with rotation.

## Example 7-12. Combined rotation and sinusoidal reciprocation in presence of mudpump flow rate ramp-up for yield stress fluid.

This comprehensive example illustrates the high level of simulation complexity offered by the math model. Here we again consider an eccentric annulus, however, now containing a Herschel-Bulkley yield stress fluid. The drillpipe is allowed to axially reciprocate sinusoidally in time, while rotation rate increases linearly with time. The mudpump pressure gradient is allowed to steepen with time from start-up to describe increased pumping action. All of these effects are coupled nonlinearly. They can be computed quickly and stably, and if numerical instabilities are encountered, they can be remedied by decreasing time step size. To accommodate this possibility, the algorithm is efficiently coded to make optimal use of memory resources and will allow up to 10,000,000 time steps, for which calculations may require about fifteen minutes or more. The assumptions are shown in Figure 7-12a, while detailed pipe displacement histories, applied pressure gradients and computed volume flow rate are given in Figure 7-12b.

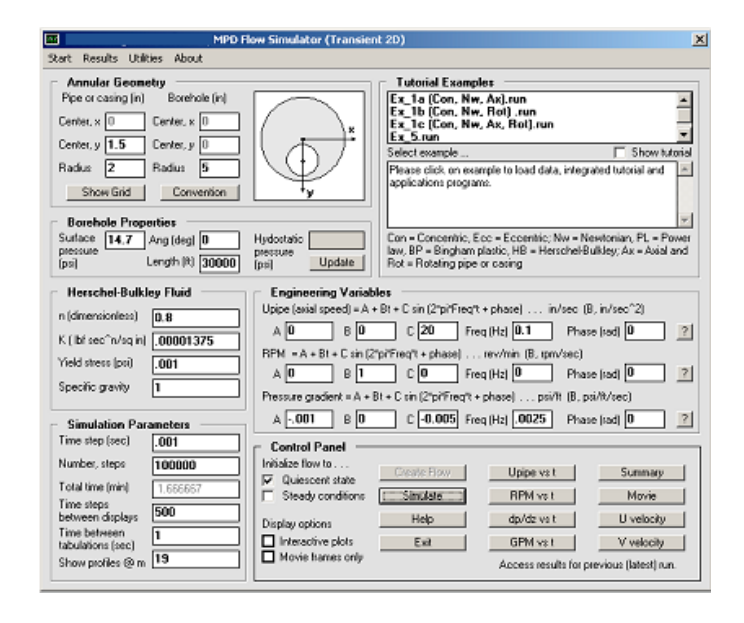


**Figure 7-12a.** Basic assumptions, comprehensive example.

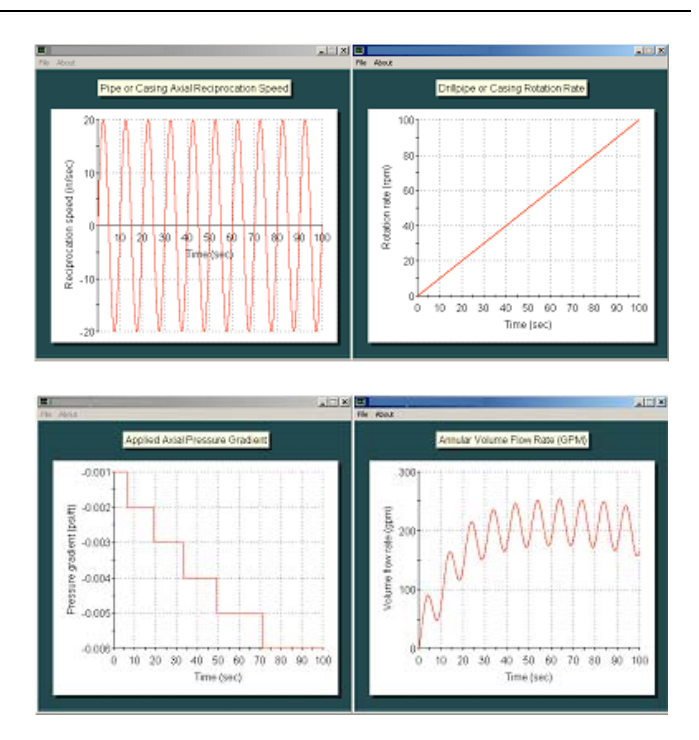


**Figure 7-12b.** Additional assumptions and computed flow rate with time.

**Preface to Example 7-4.** The foregoing examples address pipe rotation in eccentric holes. Again, for such problems, a nonlinear convective term (proportional to density and rpm, and inversely proportional to viscosity) basically alters the effective pressure gradient "seen" by the governing equation. For eccentric flows, numerical methods are required, and we have used boundary-conforming curvilinear grids in the implementations. When the underlying annular geometry is concentric, it turns out that closed form analytical solutions can be developed for power law flows.

### Example 7-4. Effect of steady rotation for laminar power law flows in concentric annuli.

In this example, we use the closed form analytical solution developed for steady, rotating, power law fluids in concentric annuli to explore pressure gradient and flow rate relationships in a non-Newtonian application. The user interface is shown in Figure 7-4a where the third option is selected. Using automatically defined internal parameters, this simulation plots flow rate (gpm) on the vertical axis and pressure gradient (dp/dz) and rotation rate (rpm) on the two horizontal axes, as shown in Figure 7-4b. It is clear from this figure that as the (absolute value of) pressure gradient increases for fixed rpm, flow rate increases, as would be expected. Interestingly, as the rotation rate increases at fixed dp/dz, the flow rate also increases. This is explained by the reduction in apparent viscosity induced by rotation due to shear-thinning.

This result also appears in several related and well known investigations external to the petroleum industry. It is,

importantly, consistent with the results of classical studies in Bird, Armstrong and Hassager (1987). Their Example 4.2-5 conclusion "shows that the flow in the axial direction is enhanced because of the imposed shearing in the tangential direction, since this additional shearing causes the viscosity to be lowered." The numerical analysis by Savins and Wallick (1966) also supports the findings. From their Abstract, "the most interesting consequence of the coupling effect is that the axial flow resistance is lowered in a helical flow with the result, for example, that for a given applied axial pressure gradient, the axial discharge rate in a helical flow field is higher than in a purely annular flow field." In the analysis, the authors observe that "it is seen that the effect of a helical flow produced by impressing a relative rotation on the z directed annular flow is to increase the axial discharge rate. This result is not unexpected. The preceding viscosity profile analyses showed that the shear-dependent viscosity is lowered, hence the axial flow resistance is lowered." Finally, from their Summary, "in contrast, if the fluid were Newtonian the superimposed laminar flows would be noninterfering in that there would be no coupling among the discharge rate, axial pressure gradient, relative rotation, and torque through the viscosity coefficient." Recall that we have proven this latter observation directly from the governing Navier-Stokes equations. Several subsequent theoretical and experimental petroleum publications also support the foregoing results.

It is important to emphasize that, in all of the above works and in the present Example 7-4, laminar, concentric annular flows are considered. For concentric flows, the nonlinear inertia (or convective) terms in the governing momentum equations vanish identically and velocity coupling is possible only through changes to apparent viscosity or shear-thinning. Early publications focused, fortuitously, on this limit – from the mathematical perspective, for simplicity, and from the drilling perspective, by the vertical well applications prior to 1990. In the past two decades, with deviated and horizontal wells becoming predominant in exploration, conflicting relationships between pressure gradient and flow rate have been reported. These conflicts arise because of annular eccentricity. In general non-Newtonian flows, shear-thinning is always present; however, when eccentricity exists, the applied pressure gradient is effectively modified by a spatially-dependent convective term that is proportional to fluid density and rotation rate. The complicated interplay between flow rate, applied pressure gradient, fluid rheology, rotation rate and annular geometry cannot be described by casual "rules of thumb," however, it can be obtained as the solution of coupled nonlinear partial differential equations.

Let us return for now to concentric annular flow analysis. Figure 7-4c provides a different view of the results from that provided by Figure 7-4b. It is obtained by selecting the last option in Figure 7-4a. Note that each figure uses hundreds of solution points, and both are produced, because analytical solutions are used, in less than one second of computing time. Again, the increase in flow rate (for a fixed pressure gradient)

obtained when rotation rate increases is well accepted in the older literature, but confusion and inconsistencies have arisen in recent studies, a point we address in several examples next.

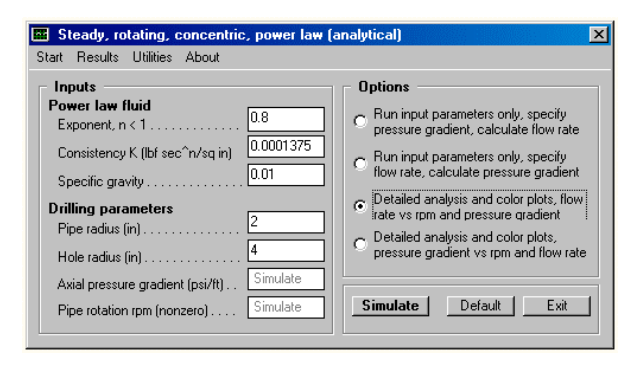
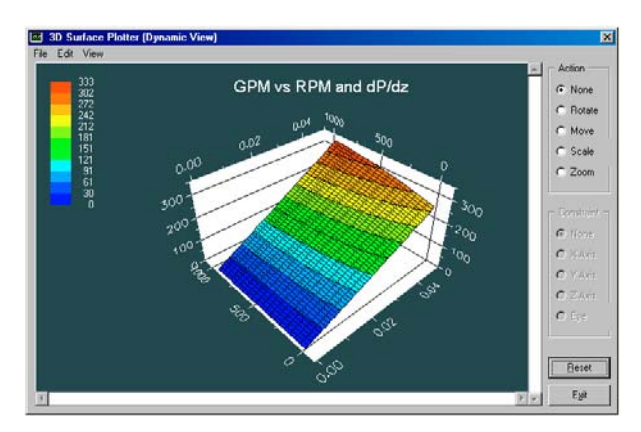


Figure 7-4a. Steady, rotating, power law simulator.



**Figure 7-4b.** GPM vs RPM and dp/dz.

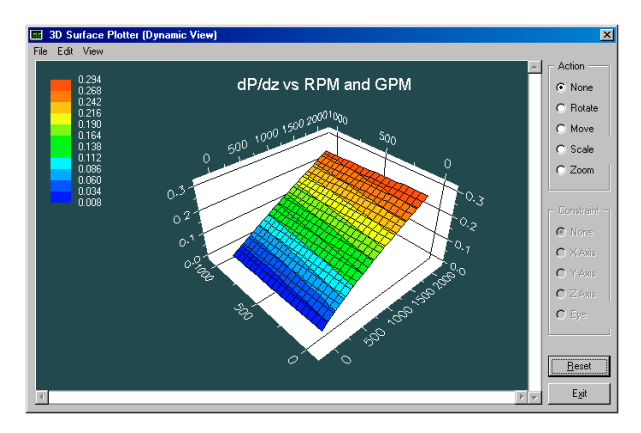


Figure 7-4c. dp/dz vs RPM and GPM.

**Supporting simulator, Model 5-3.** The model in Example 7-4 above deals with power law flows in concentric annuli with inner pipe rotation. While the solution is analytical and in closed form, it is not exact, since (reasonable) approximations were made to facilitate solution, e.g., replacing values of certain functions by midpoint values. On the other hand, a completely *exact* solution for general Herschel-Bulkley fluids with non-zero yield stresses can be developed for non-rotating flow in concentric annuli without

approximation. Essentially, when the pressure gradient, yield stress, and inner and outer radii are given (in the obvious nomenclature below), the constant C found from the (relatively simple) solution of

is used to evaluate the formulas below for the sheared zones on either side of the cylindrical ring plug. These, in turn, are used to compute exact volume flow rate.

$$\begin{split} U(r) = & + (1/K) \int \frac{R_o}{\left( - \frac{1}{2} \ dp/dz \ r \ + C/r - \tau_{yield} \right)^{-1/n} \ dr \\ r \end{split}$$
 
$$U(r) = & + (1/K) \int \frac{r}{\left( \frac{1}{2} \ dp/dz \ r \ - C/r - \tau_{yield} \right)^{-1/n} \ dr \\ R_i \end{split}$$

**Software interface and typical results.** The model derived here is called and executed from the steady flow user interface under the "Utility" sub-menu. The complete output file under the assumptions shown is duplicated below.

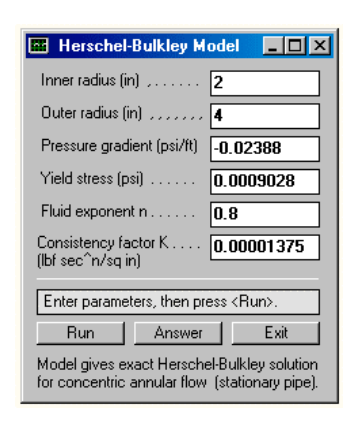


Figure 5-3b. Exact Herschel-Bulkley concentric model.

An example of the output from the Herschel-Bulkley solver is shown below.

```
Herschel-Bulkley (Concentric) Annulus Model:
Exact solution to differential equations ...

INPUT SUMMARY
Inner annular radius (in): 0.2000E+01
Outer annular radius (in): 0.4000E+01
Pressure gradient (psi/ft): -.2388E-01
Fluid exponent n (dimless): 0.8000E+00
Fluid yield stress (psi): 0.9028E-03
K factor (lbf sec^n/sq in): 0.1375E-04

Plug is between R = 2.5 and 3.4 in.
```

```
R = 2.0 in, U = 0.0000E+00 ft/s
R = 2.1 in, U = 0.2076E+01 ft/s
R = 2.2 in, U = 0.3513E+01 ft/s
R = 2.3 in, U = 0.4399E+01 ft/s
R = 3.6 \text{ in}, U = 0.4396E+01 \text{ ft/s}
     3.7 \text{ in, } U = 0.3762E+01 \text{ ft/s}
R = 3.8 in, U = 0.2827E+01 ft/s
R = 3.9 \text{ in, } U = 0.1577E+01 \text{ ft/s}
R = 4.0 \text{ in, } U = 0.0000E+00 \text{ ft/s}
Volume flow rate BPM: 0.1124E+02
                cuft/s: 0.1052E+01
                    GPM: 0.4719E+03
   Rad (in) Speed (ft/s)
                                  Ω
              0.0000E+00
     4.00
              0.1577E+01
     3.90
              0.2827E+01
     3.80
     3.60
              0.4396E+01
              0.4750E+01
     3.50
              0.4863E+01
     3.30
              0.4882E+01
     3.20
              0.4882E+01
     3.10
              0.4882E+01
     2.90
              0.4882E+01
     2.80
              0.4882E+01
     2.70
              0.4882E+01
     2.60
              0.4882E+01
     2.50
              0.4882E+01
     2.40
              0.4822E+01
     2 20
              0 3513E+01
              0.2076E+01
     2.10
     2.00
              0.0000E+00
```

**Figure 5-3c.** Exact velocity profile result.

**Supporting simulator, Model 5-1.** Still another *exact* solution possible is that for non-rotating Newtonian flow in a concentric annulus with arbitrary constant pipe speed which may be positive, zero or negative, e.g., Figure 5-1a. The user interface appears in Figure 5-1b.

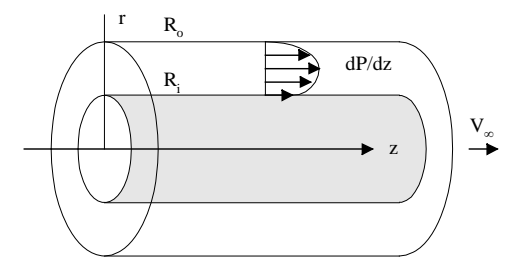


**Figure 5-1a.** Steady, concentric, Newtonian flow with moving pipe.

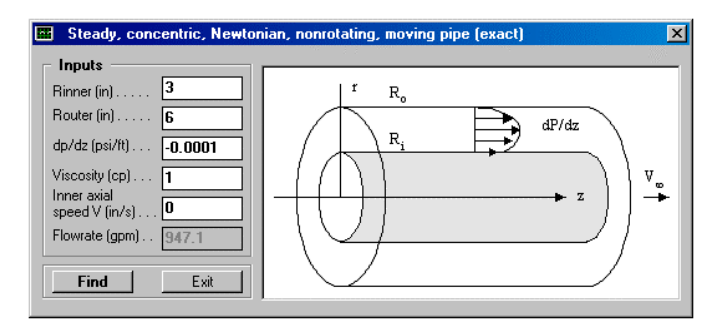


**Figure 5-1b.** Software user interface.

The exact volume flow rate used in this model is obtained from the formula

$$\begin{split} Q &= \pi \, V_{\infty} \, [(R_o^{\ 2} - R_i^{\ 2}) \, / (2 \, log_{\ e} \, (R_o/R_i)) - R_i^{\ 2} \, ] \\ &+ (\pi \, P_z \, / (8\mu)) \, [(R_o^{\ 2} - R_i^{\ 2})^{\ 2} + (R_i^{\ 4} - R_o^{\ 4}) \, log_{\ e} \, (R_o/R_i)] \, / \\ &- log_{\ e} \, (R_o/R_i) \end{split}$$

Supporting simulator, Model 5-2. In many field applications, however, density stratification is obtained when drilling stops for appreciable time periods. This is know as "barite sag." We have shown, again using analytical math models, that a single dimensionless "channel" parameter Ch controls the resulting flow, with  $Ch = U^2 \rho_{ref} / gL d\rho$  cos α (the symbols refer to flow speed, density, nominal density difference, gravity and inclination). Depending on the value of Ch, recirculating vortex zones are created within the borehole annulus which, for all practical purposes, block oncoming flow no differently than a brick would! These recirculating eddies have been observed experimentally in The required calculations, executed via the flow loops. interface in Figure 5-2-7b, involve iterative solutions of the nonlinear Euler equations, which are performed internally, within seconds. For example, streamline outputs are shown in Figures 5-2-8a,b,c which illustrate possible danger situations that may be encountered in drilling practice.

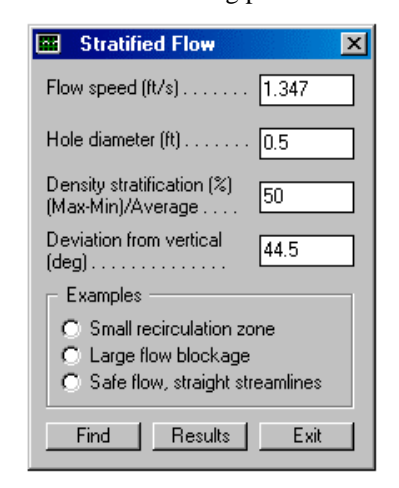


Figure 5-2-7b. Stratified flow, user interface.

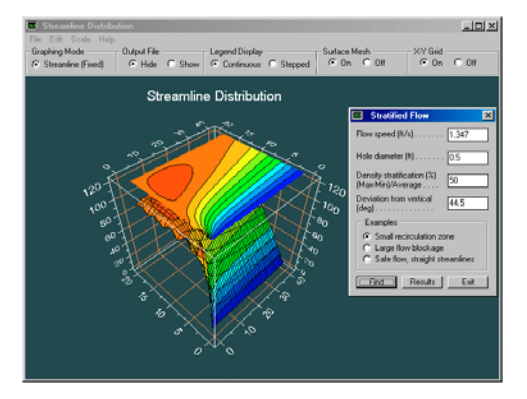


Figure 5-2-8a. Small recirculation zone.

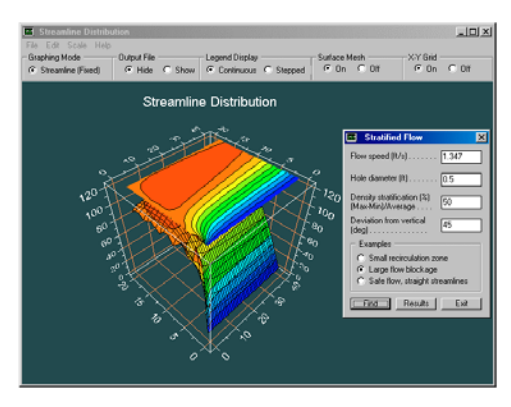


Figure 5-2-8b. Large flow blockage.

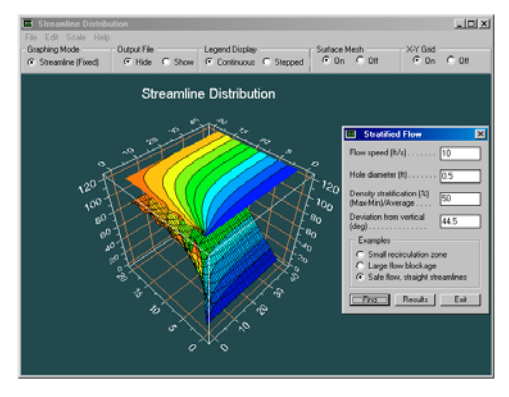


Figure 5-2-8c. Safe flow, straight streamlines.

In order to calculate pressure profiles along the hole axis inside the drillpipe and in the annulus, pipe flow solutions in addition to those for annular flow are needed. An exact solution available in the literature for Herschel-Bulkley pipe flow has been programmed in a simple utility. As will be clear later in this paper, both this pipe flow solution and the prior eccentric annular solutions, will be useful in calculating time-dependent pressure profiles along the borehole, as are obtained when multiple slugs of non-Newtonian fluid are pumped down the drillpipe following a general pump schedule. We give for reference next the exact Herschel-Bulkley pipe flow solver used in determining local pressure drops.

### Supporting simulator, Model 9-4 for Herschel-Bulkley pipe flow analysis.

As noted, the calculation of pressure at the drillbit (in the formation) and pressure along the borehole is completely determined by the distribution of pressure gradient in the hole and the value of pressure at the surface choke. If, however, the pressure needed at the mudpump to support the flow is required, also needed are the pressure loss through the drillbit as well as the pressure drop in the drillpipe. For non-rotating pipe flow, exact, closed form, circular pipe flow solutions for radial velocity distribution and total volume flow rate are available for Herschel-Bulkley fluids and have been coded in software for convenient use. Thus, the same properties for the

subsets including Newtonian, power law and Bingham plastic fluids are also available.

The general mathematical solution has been incorporated into two software programs for convenience. The first, shown in Figure 9-4-1a, solves the Equation 9-3-5d for pressure gradient when the flow rate is given. Note that this represents a nonlinear algebraic equation for the unknown. The example given here applies to a 10 cp Newtonian fluid. For the parameters shown, the required pressure gradient is about -0.001 psi/ft. In Figure 9-4-1b, we introduce yield stress to this fluid, so that it now acts as a Bingham plastic. We expect that the pressure gradient should steepen since there is greater difficulty in moving the fluid. In fact, the pressure gradient is now about – 0.015 psi/ft. Finally, in Figure 9-4-1c, we change the fluid exponent from 1.0 to 0.8, so that the fluid is now of Herschel-Bulkley type. In this case, the pressure gradient is obtained as -0.014 psi/ft. It is interesting how the presence of yield stress introduces large changes to pressure gradient over Newtonian flows.

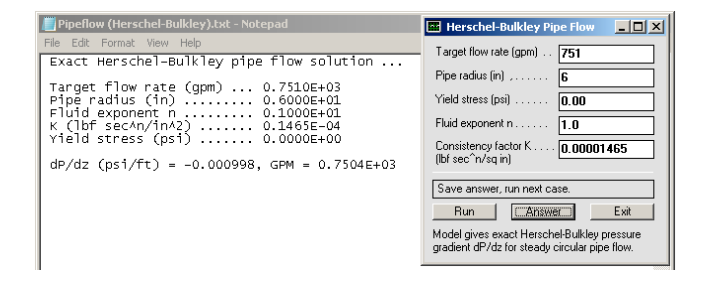


Figure 9-4-1a. Newtonian fluid, flow rate given.

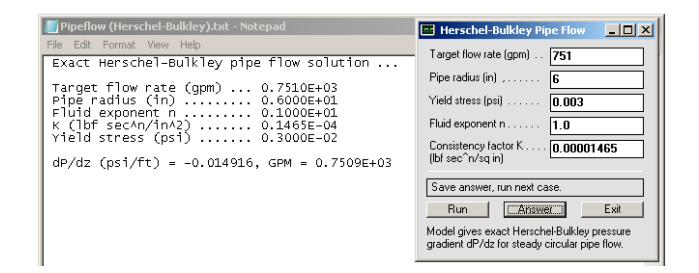


Figure 9-4-1b. Bingham plastic, flow rate given.

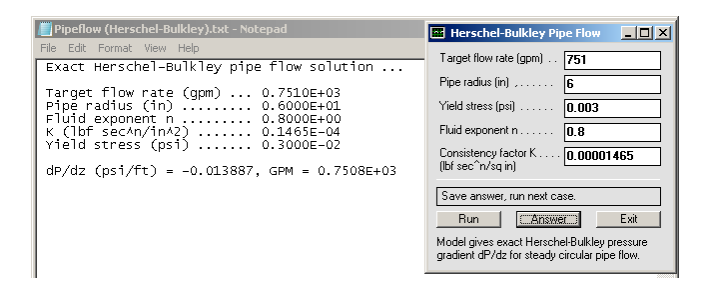
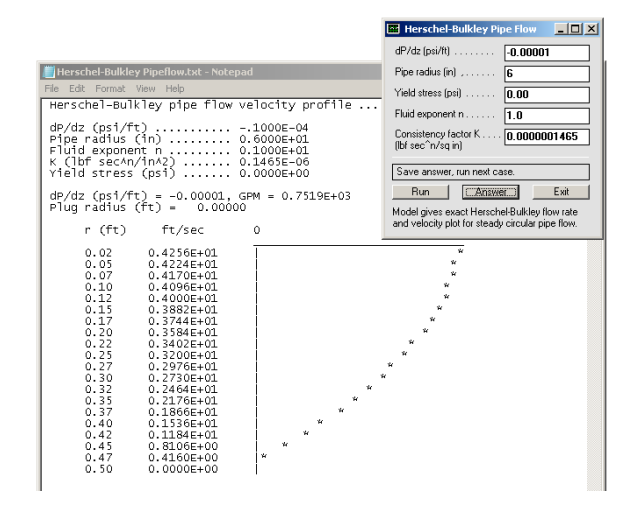


Figure 9-4-1c. Herschel-Bulkley fluid, flow rate given.

In Figure 9-4-2a, we demonstrate the second use of Equations 9-3-5a,b,c,d, namely, computing total flow rate and radial velocity distribution for any Herschel-Bulkley fluid.

Here, a Newtonian fluid is assumed, and the classic paraboloidal velocity profile is obtained. In Figure 9-4-2b, we illustrate this capability with a Herschel-Bulkley fluid. The graph clearly indicates the presence of a plug zone. The plug radius is also given in the output.



**Figure 9-4-2a.** Newtonian fluid, pressure gradient given.

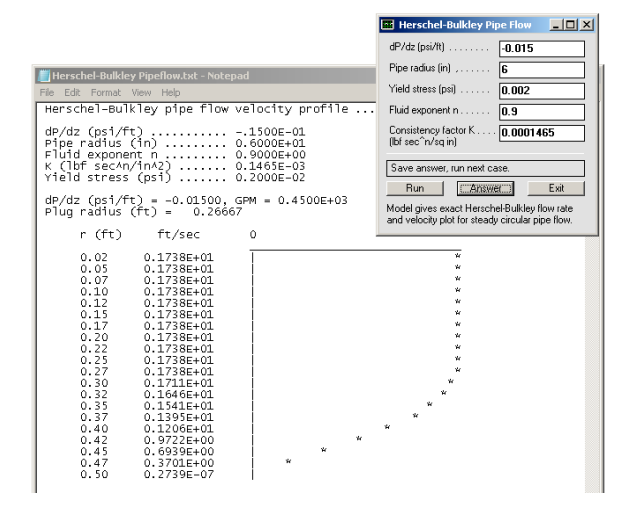


**Figure 9-4-2b.** Herschel-Bulkley fluid, pressure gradient fluid given.

# Time-Dependent Pressure Profile in Eccentric Borehole (and at Drill Bit) with Multiple Herschel-Bulkley Fluids Pumped Under General Schedule.

This section discusses the general problem shown in Figure 9-1-1. This is particularly relevant to managed pressure drilling (MPD) and also to cementing operations with combined mud, spacer and cement movement. We will discuss the figure below with regard to MPD operations. Here, multiple fluids (each with its own unique rheological properties) are pumped down the drillpipe following a general pumping schedule. Since different numbers of fluids will occupy the pipe and borehole at different times, with their positions obviously depending on time, it is clear that the

pressure distribution along the borehole (and, hence, at the drill bit) will vary with time. The problem we address is the complete pressure solution versus space and time. We note that the drilling system shown in Figure 9-1-1 can be topologically "unwrapped" into the form given in Figure 9-2-1. Hence, we turn to that diagram, which greatly simplifies the discussion (bends only introduce centrifugal effects which are modeled in the steady simulator).

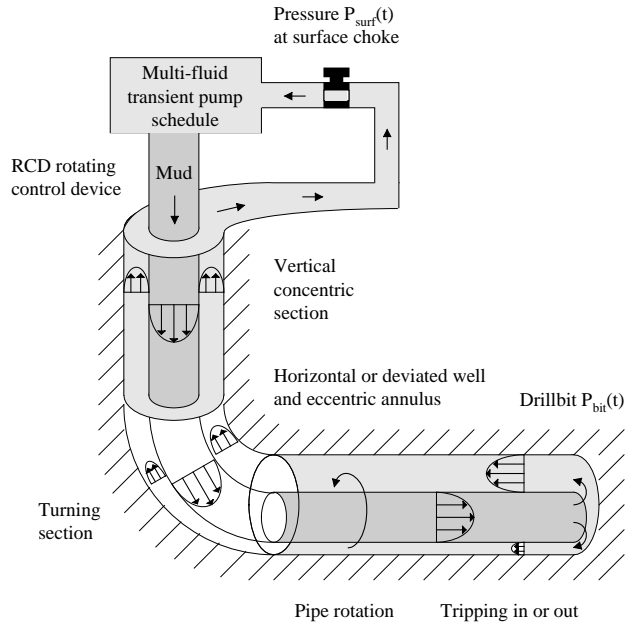


**Figure 9-1-1.** General managed pressure drilling formulation.

# Discussion 9-2. Interface tracking and total pressure drop for multiple fluids pumped in drillpipe and eccentric borehole system.

In this example, we will consider a centered or eccentered drillpipe (with cross-sectional area  $A_{\text{pipe}}$ ) located in a borehole annulus whose geometry is unchanged along its length. The annular area is  $A_{\text{annulus}}$ . Note that while pipe area is simply available from " $\pi R_{\text{pipe}}^{\ \ 2}$ ," the same is not true for the annulus if the cross-sectional contours from two initially eccentered circles have been edited to incorporate washouts, cuttings beds or fractures. If so, the "Steady 2D" simulator automatically computes and displays total cross-sectional area by summing incremental trapezoidal areas constructed from the curvilinear grid.

Now, mud progresses down the drillpipe, then out through the drillbit, and finally, flows upward in the return annulus. At the outset t=0, a single initial fluid with Herschel-Bulkley properties  $(n_0,\,K_0,\,\tau_{0,0})$  is assumed to exist in the pipe and annular system (n is the fluid exponent, K is the consistency factor, and  $\tau_0$  is the yield stress). The initial fluid may be flowing or quiescent. At t=0+, the mud pump starts to act according to a user-defined pumping schedule with piecewise constant rates. At  $t=t_0=0+$ , Fluid "1" with properties  $(n_1,\,K_1,\,\tau_{0,1})$  is pumped into the pipe at the volume

flow rate of  $Q_1$ , while at  $t=t_1$ , a second Fluid "2" with properties  $(n_2,\,K_2,\,\tau_{0,2})$  is pumped at rate  $Q_2$ , and so on. In fact, we have

- Fluid "1" pumped at rate  $Q_1$ :  $t_0 \le t < t_1$
- Fluid "2" pumped at rate  $Q_2$ :  $t_1 \le t < t_2$
- Fluid "3" pumped at rate  $Q_3$ :  $t_2 \le t < t_3$
- Fluid "4" pumped at rate  $Q_4$ :  $t_3 \le t < t_4$
- Fluid "5" pumped at rate  $Q_5$ :  $t \ge t_4$

The overall pumping process is illustrated at the top of Figure 9-2-1. Here, fluid introduced at the far right into the drillpipe travels to the left, and then turns at the drillbit (not shown), and finally progresses to the very far right. The middle diagram shows five interfaces (starting at t<sub>0</sub>, t<sub>1</sub>, t<sub>2</sub>, t<sub>3</sub> and t<sub>4</sub>) associated with the onset of each pump actions. The location "z<sub>1</sub>" (using the "little z" left-pointing coordinate system shown) describes the interface separating the initial fluid ahead of it with Fluid "1" just behind it. Similarly, "z<sub>2</sub>" separates Fluid "1" ahead of it and Fluid "2" behind it. The last Fluid "5" is a single fluid that is pumped continuously without stoppage with flow rate  $Q_5$  for  $t \ge t_4$ . While more interfaces are easily handled programming-wise, a limit of five (which models six fluid slugs) to enable rapid modeling and job prototyping, was assumed, since this number suffices for most rigsite planning purposes. Once the first interface reaches the end of the drillpipe, shown with length L, that is,  $z_1 = L$ , it turns into the borehole annulus and travels to the right. Similar descriptions apply to the remaining interfaces. Annular interfaces are described by the "big Z" right-pointing coordinate system at the bottom in Figure 9-2-1. When  $Z_1 =$ L, the first fluid pumped will have reached the surface.

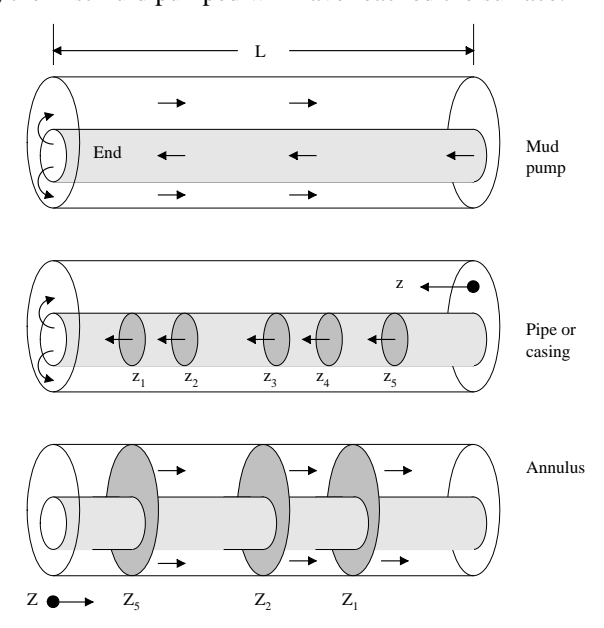


Figure 9-2-1. General pumping schedule.

Figure 9-2-1 provides a "snapshot" obtained for a given instant in time. At different times, the locations of the interfaces will be different, and pressure profiles along the

borehole (and hence, at the drillbit) will likewise be different. Also, while the discussion focuses on drilling applications with distinct mud interfaces, it is clear that all of the results apply to cement-spacer-mud systems.

Now, we wish to determine the locations of  $z_{1,2,3,4,5}$  and  $Z_{1,2,3,4,5}$  as functions of time. In general, this is a difficult problem if the fluids are compressible, or if significant mixing is found at fluid interfaces, or both. However, if the lengths of the fluid slugs are long compared to the annular diameter (so that mixing zones are not dynamically significant), and further, if the pump acts instantaneously and transient fluid effects reach equilibrium quickly, interface tracking can be accomplished kinematically. Once the locations of all interfaces are known for any instant in time, pressure drop calculations (for each fluid slug) proceed using the non-Newtonian flow models developed previously.

Two output tables are provided by the "interface tracker." The calculations are performed almost instantaneously by the software model. The two are, respectively, "Drillpipe Fluid Interfaces vs Time" and "Annular Fluid Interfaces vs Time," as shown in Figures 9-2-2 The numbers assumed for these tables are obviously not realistic, and for this reason, the units shown in the headings should be ignored for now. They were chosen so that all results fit on the printed page, with all values allowing convenient visual checking and understanding of the computer output.

ELAPSED Minutes	TIME Hours	FLOW GPMs	Dril z(1)	llpipe Fl z(2)	uid Inte	rface (i	feet) z(5)
0	0.	1	0	0	0	0	0
1	0.	1	1	0	0	0	0
2	0.	1	2	0	0	0	0
3	0.	1	3	ō	ō	ō	0
4	0.	1	4	Ö	Ö	Ö	0
-	٠.	-	-	Ü	Ü	ŭ	ŭ
5	0.	2	5	0	0	0	0
6	0.	2	7	2	0	0	0
7	0.	2	9	4	0	0	0
8	0.	2	11	6	0	0	0
9	0.	2	13	8	0	0	0
1.0		-	1.5	7.0	•		
10	0.	3	15	10	0	0	0
11	0.	3	18	13	3	0	0
12	0.	3	21	16	6	0	0
13	0.	3	24	19	9	0	0
14	0.	3	27	22	12	0	0
15	0.	4	30	25	15	0	0
16	0.	4	34	29	19	4	0
17	0.	4	38	33	23	8	0
18	0.	4	42	37	27	12	0
19	0.	4	46	41	31	16	0
0.0		_		4.5	2.5		
20	0.	5	50	45	35	20	0
21	0.	5	55	50	40	25	5
22	0.	5	60	55	45	30	10
23	0.	5	65	60	50	35	15
24	0.	5	70	65	55	40	20
25	0.	5	75	70	60	45	25
26	0.	5	80	75	65	50	30
27	0.	5	85	80	70	55	35
28	0.	5	90	85	75	60	40
29	0.	5	95	90	80	65	45
30	0.	5	100	95	85	70	50
31	1.	5	0	100	90	75	55
32	1.	5	0	0	95	80	60
33	1.	5	0	0	100	85	65
34	1.	5	0	0	0	90	70
35	1.	5	0	0	0	95	75
36	1.	5	0	0	0	100	80
37	1.	5	0	0	0	0	85
38	1.	5	0	0	0	0	90
39	1.	5	0	0	0	0	95
40	1.	5	0	0	0	0	100
41	1.	5	0	0	0	0	0

Figure 9-2-2. "Drillpipe Fluid Interfaces vs Time."

Note that 0's at early times along a z column indicate absence of the particular fluid in the drillpipe. Also, once the interface has reached the position "100," the end of the borehole in this illustration, the subsequent 0's are no longer meaningful and are used only to populate the table. Also, the very small annular area of  $A_{annulus}$  selected later was designed so that we can "watch fluid move" in the table of Figure 9-2-3.

ELAPSED	TIME	FLOW	Anr	ular Flu	id Inter	face (fe	et)
Minutes	Hours	GPMs	Z(5)	Z(4)	Z(3)	Z(2)	Z(1)
0	0.	1	0	0	0	0	0
1	0.	1	0	0	0	0	0
2	0.	1	0	0	0	0	0
3	0.	1	0	0	0	0	0
4	0.	1	0	0	0	0	0
5	0.	2	0	0	0	0	0
6	0.	2	0	0	0	0	0
7	0.	2	0	0	0	0	0
8	0.	2	0	0	0	0	0
9	0.	2	0	0	0	0	0
10	0.	3	0	0	0	0	0
11 12	0.	3	0	0	0	0	0
13	0. 0.	3	0	0	0	0	0
14	0.	3	0	0	0	0	0
15	0.	4	0	0	0	0	0
16	0.	4	0	0	0	0	0
17	0.	4	0	0	0	0	0
18 19	0.	4	0	0	0	0	0
19	0.	4	U	U	U	U	U
20	0.	5	0	0	0	0	0
21	0.	5	0	0	0	0	0
22	0.	5	0	0	0	0	0
23	0.	5	0	0	0	0	0
24 25	0. 0.	5 5	0	0	0	0	0
25 26	0.	5 5	0	0	0	0	0
27	0.	5	0	0	0	0	0
28	0.	5	Ö	Ö	Ö	Ö	0
29	0.	5	0	0	0	0	0
30	0.	5	0	0	0	0	0
31	1.	5	0	0	0	0	10
32	1.	5	0	0	0	10	20
33	1.	5	0	0	0	20	30
34	1.	5	0	0	10	30	40
35 <b>36</b>	1. 1.	5 <b>5</b>	0 <b>0</b>	0 <b>0</b>	20 <b>30</b>	40 <b>50</b>	50 <b>60</b>
3 <b>6</b> 37	1.	<b>5</b>	0	10	40	60	70
38	1.	5	0	20	50	70	80
39	1.	5	Ö	30	60	80	90
40	1.	5	ō	40	70	90	100
41	1.	5	10	50	80	100	0
42	1.	5	20	60	90	0	0
43	1.	5	30	70	100	0	0
44	1.	5	40	80	0	0	0
45	1.	5	50	90	0	0	0
46 47	1. 1.	5 5	60 70	100	0	0	0
47	1.	5	80	0	0	0	0
48	1.	5	90	0	0	0	0
50	1.	5	100	0	0	0	0
51	1.	5	0	Ö	ő	0	Ö

Figure 9-2-3. "Annular Fluid Interfaces vs Time."

To facilitate visual interpretation, we have assumed that  $A_{pipe}=1$  and  $A_{annulus}=0.5,\,$  so that the nominal linear displacement speeds in the pipe and annulus are  $U_{pipe}=Q/A_{pipe}$  and  $U_{annulus}=Q/A_{annulus}.$  The borehole length is assumed for clarity to be 100. At the same time, we pump according to the schedule

• Fluid "1" at a rate of  $Q_1 = 1$ :  $0 = t_0 \le t < t_1 = 5$ • Fluid "2" at a rate of  $Q_2 = 2$ :  $5 = t_1 \le t < t_2 = 10$ • Fluid "3" at a rate of  $Q_3 = 3$ :  $10 = t_2 \le t < t_3 = 15$ • Fluid "4" at a rate of  $Q_4 = 4$ :  $15 = t_3 \le t < t_4 = 20$ • Fluid "5" at a rate of  $Q_5 = 5$ :  $t \ge t_4 = 20$ 

where the five interfaces originate at t<sub>0</sub>, t<sub>1</sub>, t<sub>2</sub>, t<sub>3</sub> and t<sub>4</sub>. We next explain Figure 9-2-2. The left column provides elapsed minutes, while the second provides elapsed hours. The

volume flow rate is given in the third column. The corresponding drillpipe fluid interfaces  $z_{1,2,3,4,5}$  are given in the five remaining columns. Also, each change in flow rate (associated with a new interface) is separated by a single horizontal line spacing to enhance clarity. Consider the result for  $z_1.$  In the first time block with  $U_{\text{pipe}}=1/1=1,$  the interface advances at a rate of "1." In the second block with  $U_{\text{pipe}}=2/1,$  the interfaces advances at the rate "2." As time increases, the easily recognized rate increments are 3, 4 and 5 following the above pump schedule.

The  $z_1$  interface starts moving at t=0. Now we turn to the second interface and study the column for  $z_2$  results. At t=5, the second interface starts moving. Because we are already in the second time block, the interface moves at the rate "2." Subsequent speeds are 3, 4 and 5. Similarly,  $z_3$  starts at t=10 and rate increments with 3, followed by 4 and 5, and so on. We have described Figure 9-2-2 from the perspective of tracking individual fronts. However, the table is important for pressure calculations. Let us consider the results obtained at t=26 (these are shown in bold font for emphasis). In particular, we have

ELAPSED TIME FLOW Drillpipe Fluid Interface (feet) Minutes Hours GPMs 
$$z(1)$$
  $z(2)$   $z(3)$   $z(4)$   $z(5)$  26 0. 5 80 75 65 50 30

This printout indicates that, at t=26, the front  $z_1$  is located at z=80, while the last front  $z_5$  is located at z=30. The drillpipe thus contains six distinct fluid slugs at 100>z>80, 80>z>75, 75>z>65, 65>z>50, 50>z>30 and 30>z>0 where "100" refers to the assumed borehole length. In fact –

```
100 > z > 80 contains "initial fluid" with properties (n_0, K_0, \tau_{0,0}) 80 > z > 75 contains Fluid "1" with properties (n_1, K_1, \tau_{0,1}) 75 > z > 65 contains Fluid "2" with properties (n_2, K_2, \tau_{0,2}) 65 > z > 50 contains Fluid "3" with properties (n_3, K_3, \tau_{0,3}) 50 > z > 30 contains Fluid "4" with properties (n_4, K_4, \tau_{0,4}) 30 > z > 0 contains Fluid "5" with properties (n_5, K_5, \tau_{0,5})
```

If a non-Newtonian flow model for a Herschel-Bulkley fluid in a circular pipe were available that gave the pressure gradient  $(\partial P/\partial z)_{pipe,n}$  for any of the given fluid slugs "n" flowing at rate Q with a pipe radius  $(A_{pipe}/\pi)^{1/2}$ , then the total drillpipe pressure drop is simply calculated from (100-80)  $(\partial P/\partial z)_{pipe,0}+(80-75)$   $(\partial P/\partial z)_{pipe,1}+(75-65)$   $(\partial P/\partial z)_{pipe,2}+(65-50)$   $(\partial P/\partial z)_{pipe,3}+(50-30)$   $(\partial P/\partial z)_{pipe,4}+(30-0)$   $(\partial P/\partial z)_{pipe,5}.$  The flow rate Q used would be the one applicable at the time the snapshot was taken, in this case, Q = 5 at t = 26 (a single rate applies to all slugs at any instant in time). Now, at time t = 26, Figure 9-2-3 shows, as indicated by "0's," that none of the pumped fluids have arrived in the annulus, that is

```
ELAPSED TIME FLOW Annular Fluid Interface (feet)
Minutes Hours GPMs Z(5) Z(4) Z(3) Z(2) Z(1)
26 0. 5 0 0 0 0 0
```

Thus, the only fluid residing in the annulus is the initial fluid. If the pressure gradient obtained from an eccentric flow analysis is  $(\partial P/\partial z)_{annulus,0}$ , then the pressure drop in the annulus

is just  $(100-0)~(\partial P/\partial z)_{annulus,0}.$  If we further denote by  $\Delta$  the pressure drop through the drillbit, then the total pressure drop through the entire pipe-bit-annulus system is obtained by summing the prior three results, that is,  $(100-80)~(\partial P/\partial z)_{pipe,0}+(80-75)~(\partial P/\partial z)_{pipe,1}+(75-65)~(\partial P/\partial z)_{pipe,2}+(65-50)~(\partial P/\partial z)_{pipe,3}+(50-30)~(\partial P/\partial z)_{pipe,4}+(30-0)~(\partial P/\partial z)_{pipe,5}+\Delta+(100-0)~(\partial P/\partial z)_{annulus,0},$  which is the pressure (additive to the surface choke pressure  $P_{SURF})$  required at the mud pump to support this multi-slug flow.

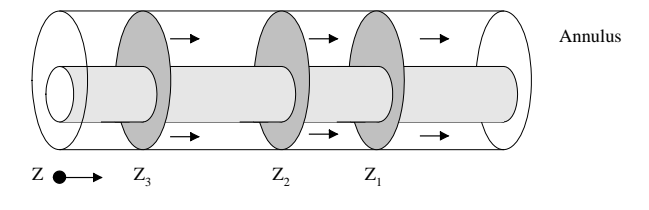
The software that creates Figure 9-2-2 also provides the times at which fluid interfaces in the drillpipe enter the borehole annulus. These are obtained from the table in Figure 9-2-2 by noting the "100" marker. In this case, we have

```
Borehole total length L, is: 100 ft. Fluid "1" enters annulus at: 30 min. Fluid "2" enters annulus at: 31 min. Fluid "3" enters annulus at: 33 min. Fluid "4" enters annulus at: 36 min. Fluid "5" enters annulus at: 40 min.
```

We next consider another time frame, say t = 36, for which the drillpipe interfaces have entered the annulus, and explain how annular pressure drops are determined, e.g., see Figure 9-2-4. For this time frame, Figure 9-2-3 gives

ELAPSED TIME FLOW Annular Fluid Interface (feet) Minutes Hours GPMs 
$$Z(5)$$
  $Z(4)$   $Z(3)$   $Z(2)$   $Z(1)$  36 1. 5 0 0 30 50 60

This indicates that three interfaces exist in the annulus, with  $Z_1$  located at the far right Z=60, followed by  $Z_2$  at Z=50 and  $Z_3$  at Z=30. Since the fluid ahead of  $Z_1$  is the "initial fluid," the total annular pressure drop is calculated from the sum (100-60)  $(\partial P/\partial z)_{annulus,0} + (60-50)$   $(\partial P/\partial z)_{annulus,1} + (50-30)$   $(\partial P/\partial z)_{annulus,2} + (30-0)$   $(\partial P/\partial z)_{annulus,3}$  where subscripts denote fluid type for the annular model.



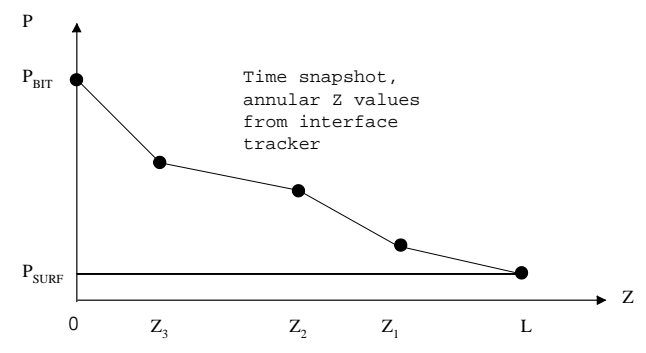
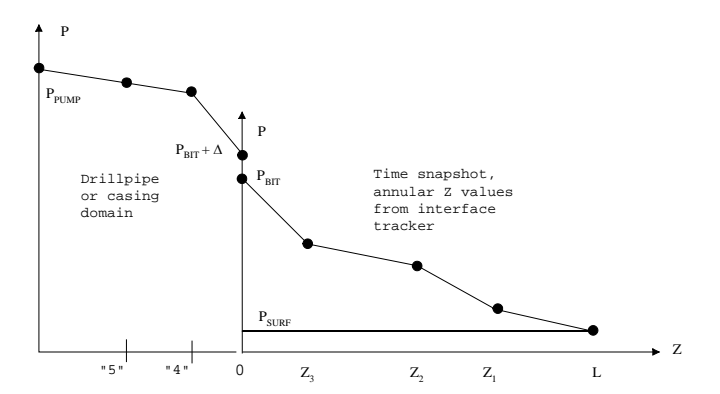


Figure 9-2-4. Example annular interface distribution.

We note that the actual pressure  $P_{BIT}$  at the drillbit in the formation is obtained by adding the total annular pressure drop to the pressure  $P_{SURF}$  obtained at the surface choke. The value

of  $P_{SURF}$  is in itself a "boundary condition," and, importantly, the pressure  $P_{BIT}$  at the bottom of the annulus *in the formation* does not depend on the pressure drop  $\Delta$  through the drillbit. On the other hand, the pressure required at the pump to move the system flow includes pipe, bit and annular losses, as shown in Figure 9-2-5 for one interface configuration.



**Figure 9-2-5.** Complete drillpipe-drillbit-annulus system.

### THREE-DIMENSIONAL, TRANSIENT, MULTIPHASE INTERFACIAL FLOW ANALYSIS

Let us recall that, for purely steady, two-dimensional, non-rotating, single-phase flow of a yield-stress or non-yield non-Newtonian fluid, the general partial differential equation below applies.

$$\partial (N \partial u/\partial y)/\partial y + \partial (N \partial u/\partial x)/\partial x = \partial P/\partial z \tag{4}$$

We again emphasize that the above equation can be easily solved in seconds for highly eccentric annuli with or without axial pipe movement, using methods based on boundary-conforming curvilinear coordinates, with either pressure gradient or volume flow rate specified, via the software implementation in Fig. 4a.

When the inner pipe rotates, the method of Fig. 4a does not apply, since the numerical solution of a purely steady formulation is unstable. Again, this does not mean that steady solutions with rotation are not possible. As demonstrated in a companion work on the effect of rotation on flowrate and pressure gradient in eccentric holes, steady, rotating flow solutions can be easily obtained as the large-time asymptotic solution of a transient formulation. This is accomplished using the code in Fig. 4d, which solves the coupled, single-phase, momentum equations in the axial and azimuthal directions on curvilinear grids, again for extended Herschel-Bulkley fluids, with or without axial pipe movement. The solution process requires seconds for low-density fluids, but for fluids denser than water, may require 2-3 minutes of computing time.

For the remainder of this paper, we will therefore assume that the axial pressure gradient on a single-phase flow basis is readily available for inner pipe that is moving both axially and azimuthally using the formulations in Fig. 4a or Fig. 4d. These pressure gradients, as we will see, provide the auxiliary conditions needed in the formulation and solution of the general transient, multiphase flow formulation in three spatial dimensions.

In the approach to the general problem for multiple slugs of non-Newtonian fluid pumped into the annulus following a general pumping schedule, we decompose the formulation into two parts. We implicitly assume that each slug of fluid is very long compared to the annular diameter. Thus, the macroscopic motion and position of all fluid interfaces can be approximately determined by the interface tracking model that we had developed earlier. Again, the model tracks more than interface positions versus time: the complete pressure profile along the borehole is available as a function of time. This therefore includes the time history of pressure at the drillbit, an important consideration for managed pressure drilling.

To obtain interfacial properties related to diffusive and convective mixing, we adopt the "boundary layer" strategy used in fluid mechanics. In flows past airplane wings, for instance, the pressure field is first determined on an inviscid flow basis; this pressure is then "impressed" across the boundary layer at the wing surface and local frictional effects satisfying a diffusion equation are then calculated.

For this problem, the interface tracking model provides the macroscopic description, one which dictates where interfaces are, and then, by applying the methods of Fig. 4a and Fig. 4d, additionally determines overall pressure histories at each location along the borehole. Now, the microscopic "boundary layer" formulation is one seeking to determine the details of the convective-diffusive mixing process in a relatively narrow zone. Unlike an aircraft boundary layer, the transition zone or mixing region here can be several feet. As in boundary layer theory, we now "zoom" into the nearfield adjacent to the interface separating two contiguous fluids, as shown in Figure 9-5-1, in a three-dimensional sense. We refer to this as the "Zoom3D" function.

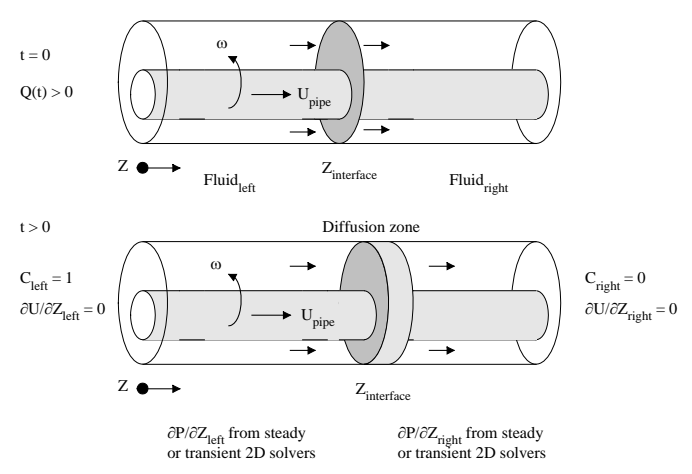


Figure 9-5-1. Transient, multiphase, boundary layer model.

The top diagram in Figure 9-5-1 shows a "left" fluid displacing a "right" fluid at t=0. The interface, per the interface tracking model, is infinitesimally thin. At later times t>0, the diagram at the bottom applies, indicating a widened mixing zone. In the nearfield model, we ask how long the

zone takes to widen and its corresponding width, which may vary across the cross-section of the annulus, and also as a function of time. The extent of multiphase fluid mixing dictates the quality in a cementing job. The multiphase problem, we might note, is not so important to drilling, but other features of the three-dimensional method may be useful in real-world drilling applications.

Mathematical formulation. Evidently, the annular flow problem is now three-dimensional, transient and multiphase. How is this modeled and solved? We obtain practical solutions following the approach first suggested by Landau and Lifschitz (1959), although modified to account for the complexities of the problem at hand. Instead of Eq. 4, we now have the transient axial momentum law in Equation 9-5-1, in which we have added a third flow direction "z" oriented axially. The left side represents nonlinear convective acceleration effects, with "v" being the azimuthal velocity function. N(C) now represents a concentration-dependent apparent viscosity function, while the pressure gradient  $\partial P/\partial z$  now varies in the z direction in a manner to be discussed. Note that the equation for "v" is similar to Equation 9-5-1.

The concentration C(x,y,z,t) satisfies the convective diffusive law in Equation 9-5-2 where  $\epsilon$  represents an empirically determined diffusion coefficient that may depend on flow rate, species or concentration (its transformed equivalent is shown in Equation 9-5-3 for reference, noting that the result for "u" takes a similar form). Note that the solutions for u, v and C are now nonlinearly coupled transient partial differential equations of parabolic type. Laboratory measurements may be used in one-dimensional experiments to determine  $\epsilon$  – then, use of this  $\epsilon$  in three-dimensional transient applications may yield important physical insights relating to the role of annular geometry.

$$\begin{split} &\rho(\partial u/\partial t + v/r \; \partial u/\partial \theta + u \; \partial u/\partial z) \; = \\ &= -\partial P/\partial z + N(C) \; (\partial^2 u/\partial x^2 + \partial^2 u/\partial y^2 + \partial^2 u/\partial z^2) + \dots (9\text{-}5\text{-}1) \\ &\partial C/\partial t + v/r \; \partial C/\partial \theta + u \; \partial C/\partial z = \\ &= -\epsilon \; (\partial^2 C/\partial x^2 + \partial^2 C/\partial y^2 + \partial^2 C/\partial z^2) \\ &\partial C/\partial t + \mathbf{q}(\; \xi \; , \; \eta \; , z) \; \cdot \; \; \nabla C = \\ &= \epsilon \; \; \left\{ C_{zz} + (\alpha C_{\xi\xi} \; - 2\beta C_{\xi\eta} \; + \gamma C_{\eta\eta} \; ) \; /J^2 \right\} \end{split}$$

**Solution strategy.** As in previous work, the differential operators in the x-y cross-space are re-expressed in curvilinear coordinates, while "z" remains "as is." Central differences are used for all spatial derivatives and backward differences are used for time derivatives in an explicit marching scheme. The boundary conditions are shown in Figure 9-5-1. Far upstream and far downstream, the velocity field is assumed to be smooth with  $\partial u/\partial z = 0$ . At the left, a "left fluid" is assumed with a concentration C = 1, while at the right, a second "right fluid" is taken with C = 0. The initial condition is shown at the top of Figure 9-5-1. At each time step, the spatial distribution of C is monitored. The front defined by the locus of points for which C = 1 travels to the right. To its left, the pressure gradient  $(\partial P/\partial z)_{left}$  obtained from the model in Fig. 4a

or Fig. 4d is used accordingly as the pipe does not or does rotate. Similarly, the pressure gradient  $(\partial P/\partial z)_{right}$  is used at the right of the interface. In a uniform fluid, the pressure gradient is constant throughout. When two contiguous slugs of fluid move at a flow rate Q, two different pressure gradients are present, since two different rheologies are present in the problem. Note that, because slug lengths are great compared to annular diameters, only two fluids (satisfying a single concentration equation) need to be treated at any given "Zoom3D" application, in contrast to the earlier work reported by the first author and his colleagues.

**Example results.** In the numerical model, we have allowed variations in borehole annular geometry in the axial direction. This is important in practical applications where the effects of anomalies like localized washouts and cuttings accumulations on velocities and viscous stresses are to be studied. Thus, in order to support three-dimensional modeling, the cross-sectional mappings are performed as needed, with transformations Jacobians and other metrics incorporated into three-dimensional arrays.

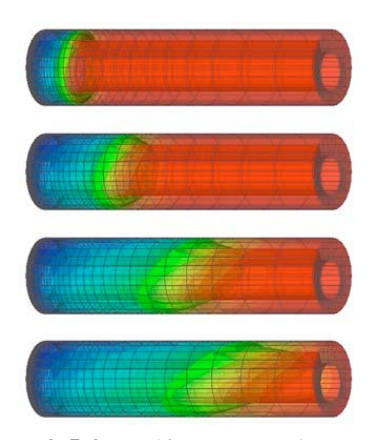
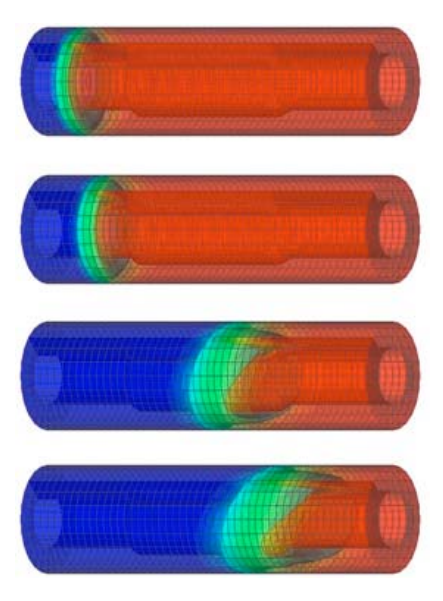


Figure 9-5-2. Uniform eccentric annulus.

Figure 9-5-2 shows the computed concentration field as a function of time, with the fluid interface propagating to the right and widening as it moves. Here, high velocities are seen at the wide side of the annulus. The amount of diffusion clearly differs azimuthally around the pipe. The annular region is clearly eccentric, but the borehole cross-section does not change with axial position. In Figure 9-5-3, we have a concentric annulus, however a highly eccentric section is introduced between the borehole ends in order to demonstrate three-dimensional effects and computational stability in the presence of sudden geometric changes. Figure 9-5-4 displays typical results from Savery, Tonmukayakul, Chin et al (2008) which support the approach used in this paper. Note that while we have plotted the concentration field as it varies with time, in order to highlight cement-mud displacement operations, we could easily have plotted the axial velocity field using color coded graphics for single-phase flow drilling applications. For horizontal drilling, the ability to model local geometric anomalies, e.g., cuttings beds, washouts, and so on, supports well stability and hole cleaning planning activities.



**Figure 9-5-3.** Concentric annulus with embedded eccentric section.



**Figure 9-5-4.** Experimental results, Savery, Tonmukayakul, Chin *et al* (2008).

User interface. As noted, e.g., refer to the formulation outlined in Figure 9-5-1, for general non-Newtonian flows with pipe rotation, inputs to multiphase calculations include pressure gradients obtained from the detailed calculations in Fig. 4a and 4d. User interface design is complicated by these auxiliary requirements and the aim is an easy-to-use software environment that solves this near-field problem as well as the macroscopic interface tracking automatically. In order to be completely transparent to the user, the interface logic must be capable of detecting slow convergence (or non-convergence) and correct for this without human intervention. This is presently an area of active work. While important, the task is straightforward and involves programming only. Newtonian mixtures, the availability of exact scaling laws automates the computations. The interface in Figure 9-5-5, for example, allows introduction of borehole anomalies in the geometry definition with online editing, and also, provides "on demand" movie playback of all physical properties in addition to detailed tabulations. The menus in Figures 4a, 4d and 9-5-5 are called from a central menu. The complete system will integrate all of these software elements.

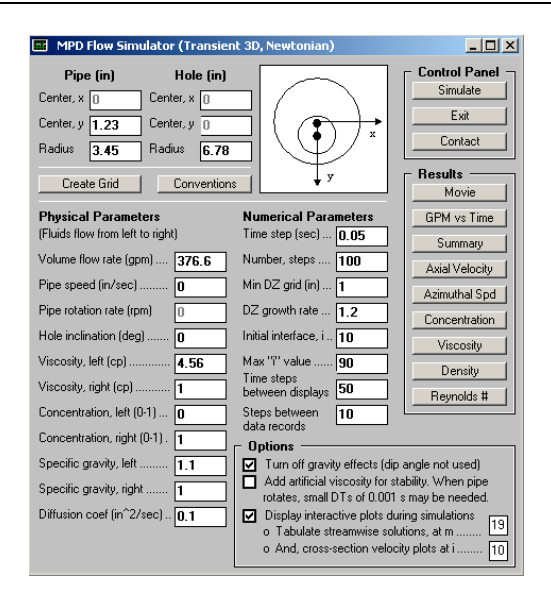


Figure 9-5-5. Candidate multiphase flow user interface.

More general problems. An additional, more general, two-part interface has been developed for non-Newtonian flow problems with or without rotation. This is accessed from the high-level menu of Fig. 9-5-6. The first menu is shown in the foreground of Fig. 9-5-7 and accepts inputs related to the pumping schedule and the fluid rheologies associated with each pump interval. For example, two distinct pressure gradients would be inputted to model the displacement of one fluid by another. The second menu is shown in the background and accepts inputs related to annular geometry definition and simulaton parameters.



**Figure 9-5-6.** High level transient, 3D, multiphase menu.

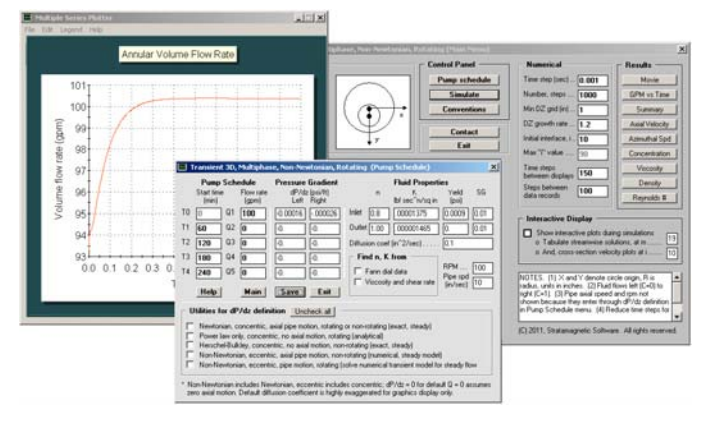
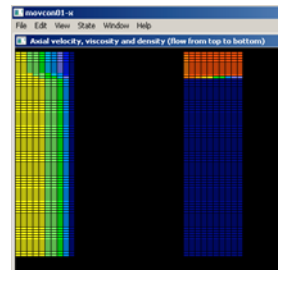
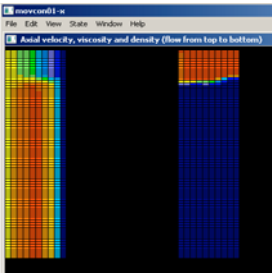
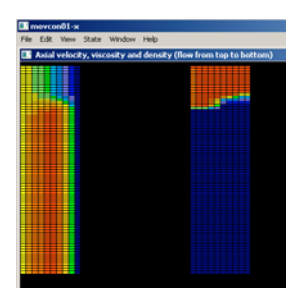
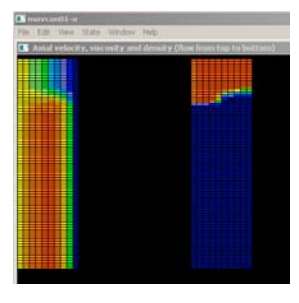


Figure 9-5-7. Transient, 3D, two-phase mixture formulation.









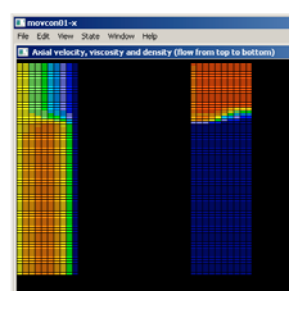


**Figure 9-5-8.** Axial velocity (left), apparent viscosity (right), flow moving downward in each frame, time increases downward from frame to frame.

■ Ans-Vis-X.dat - Notepad										
File I	File Edit Format View Help									
	e (sec): 1 0.997E+02 0.101E+03 0.101E+03 0.101E+03 0.101E+03 0.101E+03 0.101E+03	9.0 2 0.913E+02 0.943E+02 0.996E+02 0.100E+03 0.101E+03 0.101E+03	3 0.913E+02 0.943E+02 0.996E+02 0.100E+03 0.100E+03 0.101E+03 0.101E+03	4 0.913E+02 0.943E+02 0.996E+02 0.100E+03 0.100E+03 0.101E+03 0.101E+03	5 0.913E+02 0.943E+02 0.996E+02 0.100E+03 0.100E+03 0.101E+03 0.101E+03	6 0.913E+02 0.943E+02 0.996E+02 0.100E+03 0.100E+03 0.101E+03 0.101E+03	7 0.913E+02 0.943E+02 0.996E+02 0.100E+03 0.100E+03 0.101E+03 0.101E+03			
9 10 11	0.101E+03 0.101E+03 0.101E+03	0.101E+03 0.101E+03 0.101E+03	0.101E+03 0.101E+03 0.101E+03	0.101E+03 0.101E+03 0.101E+03	0.101E+03 0.101E+03 0.101E+03	0.101E+03 0.101E+03 0.101E+03	0.101E+03 0.101E+03 0.101E+03			
I										

I	Mans-Vis-X.dat - Notepad									
	File Edit Format View Help									
	87 0.100E+02 0.100E+02 0.100E+02 0.100E+02 0.100E+02 0.100E+02 0.100E+02 0.100E+02 0.100E+02 0.100E+02 0.100E+02	88 0.100E+02 0.100E+02 0.100E+02 0.100E+02 0.100E+02 0.100E+02 0.100E+02 0.100E+02 0.100E+02 0.100E+02 0.100E+02	89 0.100E+02 0.100E+02 0.100E+02 0.100E+02 0.100E+02 0.100E+02 0.100E+02 0.100E+02 0.100E+02 0.100E+02 0.100E+02	90 0.100E+02 0.100E+02 0.100E+02 0.100E+02 0.100E+02 0.100E+02 0.100E+02 0.100E+02 0.100E+02 0.100E+02 0.100E+02						

**Figure 9-5-9.** Apparent viscosity for "constant m" or azimuthal angle.

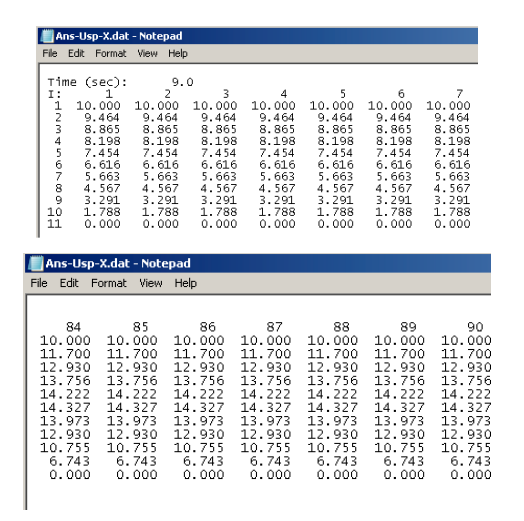


Figure 9-5-10. Axial velocity solution.

_	Ans-Yth-X.dat - Notepad								
File E	File Edit Format View Help								
Tim I: 1 2 3 4 5 6 7 8 9	e (sec): 1 0.314E+02 0.277E+02 0.242E+02 0.208E+02 0.176E+02 0.114E+02 0.851E+01 0.564E+01 0.281E+01 0.000E+00	9.0 2 0.314E+02 0.277E+02 0.242E+02 0.208E+02 0.176E+02 0.114E+02 0.851E+01 0.564E+01 0.281E+01 0.000E+00	3 0.314E+02 0.277E+02 0.242E+02 0.208E+02 0.176E+02 0.114E+02 0.851E+01 0.564E+01 0.281E+01 0.000E+00	4 0.314E+02 0.277E+02 0.242E+02 0.208E+02 0.176E+02 0.114E+02 0.851E+01 0.564E+01 0.281E+01 0.000E+00	5 0.314E+02 0.277E+02 0.242E+02 0.208E+02 0.176E+02 0.114E+02 0.851E+01 0.564E+01 0.281E+01 0.000E+00	6 0.314E+02 0.277E+02 0.242E+02 0.208E+02 0.176E+02 0.114E+02 0.851E+01 0.564E+01 0.28LE+01 0.000E+00	7 0.314E+02 0.277E+02 0.242E+02 0.208E+02 0.176E+02 0.114E+02 0.851E+01 0.564E+01 0.281E+01 0.000E+00		

Figure 9-5-11. Azimuthal velocity.

Ans-Rey-X.dat - Notepad									
File Edit Format View Help									
Time (sec): 9.0									
I:	1	2	3	4	5	6	7		
1	0.192E+01	0.209E+01	0.209E+01	0.209E+01	0.209E+01	0.209E+01	0.209E+01		
2	0.180E+01	0.192E+01	0.192E+01	0.192E+01	0.192E+01	0.192E+01	0.192E+01		
3	0.168E+01	0.170E+01	0.170E+01	0.170E+01	0.170E+01	0.170E+01	0.170E+01		
4	0.156E+01								
5	0.141E+01	0.142E+01	0.142E+01	0.142E+01	0.142E+01	0.142E+01	0.142E+01		
6	0.125E+01	0.126E+01	0.126E+01	0.126E+01	0.126E+01	0.126E+01	0.126E+01		
7	0.107E+01								
8	0.866E+00	0.864E+00	0.864E+00	0.864E+00	0.864E+00	0.864E+00	0.864E+00		
9	0.624E+00	0.622E+00	0.622E+00	0.622E+00	0.622E+00	0.622E+00	0.622E+00		
10	0.339E+00	0.338E+00	0.338E+00	0.338E+00	0.338E+00	0.338E+00	0.338E+00		
11	0.000E+00								

Figure 9-5-12. Reynolds number, very low, stable flow.

On completion of the transient, three-dimensional, multiphase simulation, different types of outputs are available. For instance, Figure 9-5-8 captures movie frames showing the timewise evolution of the velocity and apparent viscosity fields in an azimuthal plane specified by the user. Movies are accessed by clicking the "Movie" button in Figure 9-5-7. The same menu also provides direct access to numbers, and typical screens are shown in Figures 9-5-9 to 9-5-12. Note that the very low Reynolds numbers shown in the last printout indicate fluid stability on a single-phase flow basis. The fluid interface in the above movie frames is seen to widen gradually as it convects downward.

#### **Closing Remarks**

The present paper describes new capabilities in modeling steady and transient non-Newtonian flow in highly eccentric annuli, with or without plug zones associated with yield stress fluids, with realistic geometric anomalies, plus effects like borehole axis curvature and drillpipe translation and rotation. Numerous models were described, together with example calculations, to show how pressure gradients can be computed effortlessly using well-posed mathematical formulations hosted by easy-to-user software interfaces. These "building block" capabilities are, of course, by themselves useful. However, they were created with the more important goal in mind – that of calculating the time-dependent pressure along the complete borehole (which includes time-history at the drillbit) as it would depend on multiple non-Newtonian fluids pumped into the drillpipe following a general pump schedule. Here, the intricacies of interface tracking were addressed, and these time histories were integrated with solutions obtained separately by evaluating the building blocks previously discussed. We also demonstrated how details of the mixing interface between two long slugs of fluid can be determined by solving a convective-diffusive equation system. We also emphasize that, in all of the models, detailed distributions of physical properties like axial velocity, rotational velocity, apparent viscosity, shear rate and viscous stress are available to the user "on demand." These properties may be useful for correlation purposes and perhaps will aid in understanding a particular physical phenomenon of curiosity.

### Acknowledgments

The authors gratefully acknowledge 2009-2011 support from the United States Department of Energy for their technical proposal "Advanced Steady-State and Transient, Three-Dimensional, Single and Multiphase, Non-Newtonian Simulation System for Managed Pressure Drilling." We are indebted to Art Schroeder, Energy Valley, to Jim Chitwood, Chevron, and to James Pappas, RPSEA, for their encouragement and advice, and especially to John Lofton, Chevron, for his engineering insights and guidance related to several areas of the modeling of rotating pipe flow effects. The views expressed in this paper represent those of the authors only and not necessarily the opinions of any program sponsors.

#### References

- Bird, R.B., Armstrong, R.C., and Hassager, O., <u>Dynamics of Polymeric Liquids</u>, <u>Volume 1: Fluid Mechanics</u>, John Wiley & Sons, New York, 1987.
- Chin, W.C., <u>Borehole Flow Modeling in Horizontal</u>, <u>Deviated and Vertical Wells</u>, Gulf Publishing, Houston, 1992.
- 3. Chin, W.C., <u>Computational Rheology for Pipeline and Annular Flow</u>, Elsevier, Cambridge, 2001.
- 4. Chin, W.C., <u>Quantitative Methods in Reservoir Engineering</u>, Elsevier, Cambridge, 2002.
- Chin, W.C. and Zhuang, X., "Exact Non-Newtonian Flow Analysis of Yield Stress Fluids in Highly Eccentric Borehole Annuli with Pipe or Casing Translation and Rotation," SPE 131234-PP, presented at the CPS/SPE International Oil & Gas Conference and Exhibition, Beijing, China, 8-10 June 2010.
- 6. Landau, L.D. and Lifschitz, E.M., <u>Fluid Mechanics</u>, Pergamon Press, London, 1959.
- Savery, M., Tonmukayakul, P., Chin, W.C., Deawwanich, T., Liew, J. and Q. D. Nguyen, "Laminar Displacement of Viscoplastic Fluids in Eccentric Annuli – Numerical Simulation and Experimental Validations," XXII International Congress of Theoretical and Applied Mechanics (ICTAM 2008), Adelaide, Australia, Aug. 24-29, 2008.
- 8. Savins, J.G., and Wallick, G.C., "Viscosity Profiles, Discharge Rates, Pressures, and Torques for a Rheologically Complex Fluid in a Helical Flow," *A.I.Ch.E. Journal*, Vol. 12, No. 2, March 1966, pp. 357-363.
- Souza Mendes, P.R. and Dutra, E.S.S., "A Viscosity Function for Viscoplastic Liquids," Annual Transactions of the Nordic Rheology Society, Vol. 12, 2004.